






















RESEARCH ARTICLE | AUGUST 22 2025

Single-shot in-line x-ray phase-contrast imaging of void-shockwave interactions in fusion energy materials

Special Collection: [Progress in Inertial Fusion Energy Research: Two Years After Ignition](#)

D. S. Hodge ; A. F. T. Leong ; K. Kurzer-Ogul ; S. Pandolfi ; D. S. Montgomery ; J. Shang ; H. Aluie ; S. Marchesini ; Y. Liu ; K. Li ; A. Sakdinawat ; E. C. Galtier ; B. Nagler ; H. J. Lee ; E. F. Cunningham ; T. E. Carver ; C. A. Bolme ; K. J. Ramos; D. Khaghani ; P. M. Kozłowski ; A. E. Gleason ; R. L. Sandberg 



Phys. Plasmas 32, 083903 (2025)

<https://doi.org/10.1063/5.0272820>

 CHORUS



Articles You May Be Interested In

Radiation and heat transport in divergent shock–bubble interactions

Phys. Plasmas (March 2024)

Role of self-generated magnetic fields in the inertial fusion ignition threshold

Phys. Plasmas (July 2022)

Coupling multi-fidelity xRAGE with machine learning for graded inner shell design optimization in double shell capsules

Phys. Plasmas (June 2023)

24 August 2025 19:48:29

Single-shot in-line x-ray phase-contrast imaging of void-shockwave interactions in fusion energy materials

Cite as: Phys. Plasmas **32**, 083903 (2025); doi: [10.1063/5.0272820](https://doi.org/10.1063/5.0272820)

Submitted: 26 March 2025 · Accepted: 26 July 2025 ·

Published Online: 22 August 2025



View Online



Export Citation



CrossMark

D. S. Hodge,^{1,2,a)} A. F. T. Leong,³ K. Kurzer-Ogul,^{3,4} S. Pandolfi,^{5,6} D. S. Montgomery,³ J. Shang,^{4,7} H. Aluie,^{4,7,8} S. Marchesini,⁶ Y. Liu,⁶ K. Li,⁶ A. Sakdinawat,⁶ E. C. Galtier,⁶ B. Nagler,⁶ H. J. Lee,⁶ E. F. Cunningham,⁶ T. E. Carver,⁹ C. A. Bolme,³ K. J. Ramos,³ D. Khaghani,⁶ P. M. Kozlowski,³ A. E. Gleason,^{1,6} and R. L. Sandberg^{1,2}

AFFILIATIONS

¹DOE IFE-STAR RISE-Hub, Fort Collins, Colorado 80523, USA

²Department of Physics and Astronomy, Brigham Young University, Provo, Utah 84602, USA

³Los Alamos National Laboratory, Los Alamos, New Mexico 87545, USA

⁴Department of Mechanical Engineering, University of Rochester, Rochester, New York 14623, USA

⁵Sorbonne Université, Muséum National d'Histoire Naturelle, UMR CNRS 7590, Institut de Minéralogie, de Physique des Matériaux et de Cosmochimie, IMPMC, 75005 Paris, France

⁶SLAC National Accelerator Laboratory, 2575 Sand Hill Rd., Menlo Park, California 94025, USA

⁷Laboratory for Laser Energetics, University of Rochester, Rochester, New York 14623, USA

⁸Department of Mathematics, University of Rochester, Rochester, New York 14623, USA

⁹Stanford University, Stanford Nano Shared Facilities, Stanford, California 94305, USA

Note: This paper is part of the Special Topic on Progress in Inertial Fusion Energy Research: Two Years After Ignition.

^{a)}Author to whom correspondence should be addressed: dhodge@byu.edu

ABSTRACT

Recent breakthroughs in nuclear fusion, specifically the report of reactions exceeding scientific breakeven at the National Ignition Facility (NIF), highlight the potential of inertial fusion energy (IFE) as a sustainable and virtually limitless energy source. However, further progress in IFE requires characterization of defects in ablator materials and how they affect fuel capsule compression. Voids within the ablator can degrade energy yield, but their impact on the density distribution has primarily been studied through simulations, with limited high-resolution experimental validation. To address this, we used the x-ray free-electron laser (XFEL) at the matter in extreme conditions (MECs) instrument at the Linac coherent light source (LCLS) to capture 2D x-ray phase-contrast (XPC) images of a void-bearing sample with a composition similar to inertial confinement fusion (ICF) ablators. By driving a compressive shockwave through the sample using MEC's long-pulse laser system, we analyzed how voids influence shockwave propagation and density distribution during compression. To quantify this impact, we extracted phase information using two phase retrieval algorithms. First, we applied the contrast transfer function (CTF) method, paired with Tikhonov regularization and a fast optimization approach to generate an initial phase estimate. We then refined the result using a projected gradient descent (PGD) method that works directly with the sample's refractive index. Comparing these results with radiation adaptive grid Eulerian (xRAGE) radiation hydrodynamic simulations enables identification of model validation needs or improvements. By calculating phase maps *in situ*, it becomes possible to reconstruct areal density maps, improving understanding of laser-capsule interactions and advancing IFE research.

© 2025 Author(s). All article content, except where otherwise noted, is licensed under a Creative Commons Attribution-NonCommercial 4.0 International (CC BY-NC) license (<https://creativecommons.org/licenses/by-nc/4.0/>). <https://doi.org/10.1063/5.0272820>

I. INTRODUCTION

Energy is fundamental to humanity, playing a crucial role in our daily lives as it revolves around its production and use.¹ Currently, the world's energy needs are met by a combination of fossil fuels—such as coal, oil, and natural gas—and cleaner alternatives, including biofuels, solar, wind, tidal, and nuclear energy. However, fossil fuels remain the dominant energy source, accounting for $\sim 80\%$ of the world's energy.^{1,2} Although cleaner methods have been promoted and are implemented in some places worldwide, each method has drawbacks and/or practical limitations.¹ Among the possible energy production methods, nuclear fusion is one of the most promising ones, since it has the potential to generate significantly more energy than all the other sources, is environmentally friendly, and the fuel is virtually limitless.

Since the 2022 breakthrough at NIF, where scientists demonstrated a yield from a nuclear fusion reaction exceeding scientific breakeven for the first time,^{3,4} followed by additional breakeven experiments,^{5–9} interest and development in fusion energy have surged both in fundamental and applied research, with potential for commercialization.^{10–12} Despite the promising results from NIF that demonstrate the viability of this approach, maximizing energy yields required for practical ICF-based powerplant applications remains a challenge due to several factors.^{11,13,14} Defects or voids in the ablator have been identified as a major contributor to energy yield degradation,^{15–20} adding an additional layer of complexity to existing challenges for future ICF-based powerplants. Maximizing energy yields necessitates the analysis of the complex, nonlinear dynamics of laser-driven compression in the fuel capsule material, particularly when defects, such as voids, are present in the ablator layer. Characterizing the interaction of laser-induced shockwaves with these defects at different stages of void collapse in an experimental setting is crucial since the underlying microphysics can drive the formation of hydrodynamic instabilities in ICF experiments,^{21,22} which must be effectively understood and mitigated to optimize energy yield.

Although several experimental studies have investigated void-shock interactions,^{23–29} further research is needed to investigate these dynamics in solid ablator materials under ICF-relevant conditions

with high resolution. Some studies have advanced ICF science by performing edge-enhanced radiographic and XPC imaging of shocked materials under ICF-relevant conditions using laser-driven backlighter sources.^{30–35} While backlighters remain a widely used diagnostic tool due to their flexibility and collocation with high power laser facilities,^{30,31} they face several limitations, including low signal-to-noise ratio, reduced spatial resolution, limited spectral brightness and coherence, and potential contamination of the image by self-emission from the target material.³³ These drawbacks can hinder the ability to resolve fine-scale features critical to understanding shock dynamics, especially with targets composed of multiple materials. Collectively, these studies have demonstrated that laser-driven XPC imaging is a promising diagnostic for high-energy-density and ICF experiments, offering enhanced sensitivity to density gradients and enabling imaging of shock fronts and material interfaces. However, in contrast to these systems, XFELs provide higher spectral brightness, superior spatial coherence, and increased spatial resolution, making them a more powerful tool for probing dynamic processes in complex, multi-material systems.

To this end, our team conducted experiments at the LCLS MEC hutch, capturing single-shot XPC images of void-shockwave interactions. In this experimental configuration (see Fig. 1), phase-contrast enhances the visibility of low-absorption samples by converting phase variations (i.e., electron density variations) into amplitude modulations on the detector. This enables high-resolution observation of subtle sample variations in the recorded images that would not be detectable via absorption-based contrast and phase retrieval reconstructions. Previous studies from the team have analyzed the physics of void collapse at extreme conditions, with key contributions from Pandolfi *et al.*,³⁶ Hodge *et al.*,³⁷ Kurzer-Ogul *et al.*,³⁸ and Leong *et al.*,³⁹ whose combined experimental and simulation efforts have established foundational work in this area. Specifically, Leong *et al.*³⁹ constructed a method to evaluate the reliability of xRAGE void collapse simulations. This approach integrated speckle-based and propagation-based XPC imaging principles into a unified phase retrieval algorithm, outperforming each technique individually. This method leveraged the

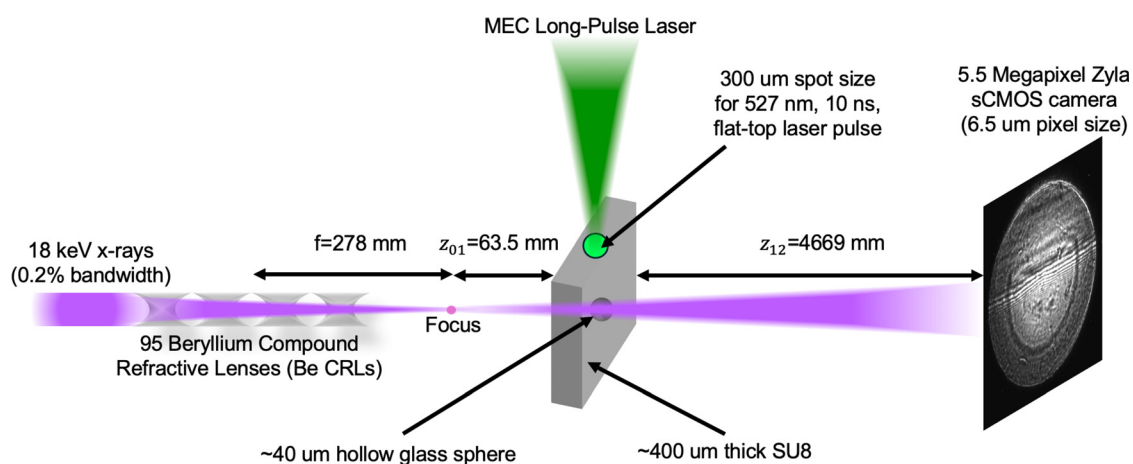


FIG. 1. Schematic of the in-line holographic XPC imaging setup where 18 keV x-rays are focused by 95 beryllium compound refractive lenses (CRLs), bringing the x-rays to a focus 278 mm after the lenses. Divergent x-rays expand out in a cone, illuminating the sample at a distance $z_{01}=63.5$ mm from the focus, and an XPC image is recorded on the Zyla camera $z_{12}=4669$ mm away from the sample. Note: This figure is not drawn to scale.

speckle pattern and phase contrast that emerge during free-space light propagation in speckle-based XPC imaging to reconstruct both the slow- and fast-varying phase features of the sample from single XPC images. The retrieved experimental phase reconstructions were then compared with the phase generated by xRAGE under the same shock conditions, highlighting similarities and discrepancies between simulation and experiment.

The work presented here builds on previous work by Leong *et al.*³⁹ In their method, a speckle pattern is required for reconstruction, but the approach presented here is broadly applicable to any setup. Specifically, we applied a phase retrieval approach that utilizes the contrast transfer function method based on the fast alternating direction method of multipliers (CTF-fADMM),^{40,41} which we used to initialize the projected gradient descent (PGD)⁴² method, to assess the accuracy of hydrodynamic simulations at these respective collapse stages. The analysis of various collapse stages is critical to develop a complete understanding of void-shock interactions and could provide insight into the details of hydrodynamic instability formation. Furthermore, we apply the method proposed here on the same dataset as Leong *et al.*³⁹ to demonstrate improvement of the simulated and experimental phase reconstructions (see Appendix B) presented in that manuscript. By comparing simulated and experimental phase reconstructions at various collapse stages, researchers can mitigate defects to increase energy yield and properly tune the simulation parameters to match experimental data.

The remainder of this paper demonstrates the effectiveness of initializing the PGD phase retrieval method with CTF-fADMM to achieve qualitatively accurate phase reconstructions. In particular, we construct a forward model using xRAGE and assess the accuracy of our phase retrieval approach by first applying it to simulated unshocked and shocked voids, where the ground truth is known. The parameters refined through these simulations are then applied to reconstruct the corresponding experimental images. By comparing reconstructions from simulation and experiment, this framework allows us to identify potential discrepancies and assess whether they arise from missing physical effects or the need for further parameter refinement within the xRAGE hydrodynamic code. We evaluated the fidelity of the phase retrieval method on the basis of its consistently strong performance across multiple cases. Section II includes sample details and describes the experimental configuration and parameters used to produce the XPC images. Next, in Sec. III, we outline the mathematical framework describing both the physical process of capturing single-shot experimental XPC images and the forward modeling of synthetic white field and sample XPC images. Using this framework, in Sec. IV, we create synthetic white-field and sample XPC images that closely replicate the characteristics of the experimental images, ensuring a high degree of accuracy in reproducing the observed data. We then applied our flat-field correction (FFC) scheme to both synthetic and experimental datasets to generate FFC XPC images, demonstrating that optimal performance requires the combined use of principal component analysis (PCA)⁴³ and image registration.⁴⁴ Finally, in Sec. V, we analyze and compare the phase retrieval results obtained from synthetic FFC XPC images with those obtained from the experimental data.

II. SAMPLE AND EXPERIMENTAL SETUP

For our laser-shock compression experiment, the samples consisted of SU-8 photoresist (1.185 g/cm^3) embedded with a hollow

SiO₂ shell (2.65 g/cm^3) as proxies to the ablator and void, respectively. A $25 \mu\text{m}$ layer of black Kapton was glued on the drive surface to mitigate the laser inhomogeneities at the ablation surface and ensure planarity of the shock front around the void. The SiO₂ shell has an outer diameter of $\sim 40 \mu\text{m}$, whereas the SU-8 photoresist layer is $\sim 400 \mu\text{m}$ thick along the x-ray beam propagation direction. These materials were selected based on their shock properties and response, which closely resemble those of materials used in ICF experiments.^{18,45,46} Additionally, the use of commercial SiO₂ shells as a proxy for voids enables precise control over the void size such that laser-shock compression can be performed with minimal variations between samples, enabling consistent reconstruction of the evolution of the system from a series of single-shot data. Although voids in actual ICF experiments are not composed of hollow SiO₂ shells, hydrodynamic xRAGE simulations indicate that ablators containing SiO₂ voids exhibit similar evolution, deformation, and polymer density compared to spherical voids at early times.³⁶ This similarity makes ablators composed of SiO₂ a suitable surrogate for experimental studies. While our experiment utilized voids larger than those typically found in ICF ablators, the early-time shock-bubble interaction (SBI) dynamics we observe remain relevant to the case of shocks interacting with ablator voids in ICF. These voids reside deep in the ICF ablator and will initially interact with the shock front before encountering the ablation front, thereby producing density perturbations as a result of classical hydrodynamic processes.²⁰ At these early times, key physical processes, such as the reflected and transmitted shock dynamics and baroclinic vorticity deposition, scale with acoustic impedance and density/pressure gradients. Although ablative stabilization plays a crucial role in suppressing instabilities originating from surface imperfections in ICF ablators, it does not prevent the growth of Rayleigh–Taylor instabilities (RTI) deeper within the ablator. There, the ablation front encounters density perturbations seeded by void-shock interactions, which can be amplified via ablative RTI. These ablation flows will move the vorticity from the void interface to the lighter of the two fluids, thereby driving jetting.⁴⁷ In this experimental work, we focus on the generation of the initial density perturbations and neglect the effect of the ablation front, which occurs at later times. Furthermore, radiation effects are negligible in our experiment, whereas in the ICF case, radiation primarily acts to modify the acoustic impedance through material preheating.³⁸ Studying void collapse at this larger scale serves as a foundational step toward constraining radiation-hydrodynamic simulations such as xRAGE. These results can be scaled to smaller voids and faster shock conditions relevant to ICF using the dimensionless time parameter²³

$$\tau = \frac{tW}{R}, \quad (1)$$

where W is the shock velocity, R is the initial radius of the void, and t is the dimensional time. In the ICF case, larger W and smaller R result in higher values of τ being reached more rapidly compared to the conditions in our LCLS experiment. The images we provide in this article show relatively small τ .

We conducted an XPC imaging experiment at the MEC instrument at LCLS. The experimental setup and parameters were the same as those described by Kurzer-Ogul *et al.*,³⁸ Pandolfi *et al.*,³⁶ and Leong *et al.*³⁹ and are illustrated in Fig. 1. Our setup employed an in-line digital holography technique, which enables high-resolution, time-resolved imaging under photon-starved conditions. This simple configuration⁴⁸

allows for single-pulse, full-field imaging with simultaneous phase and amplitude contrast.⁴³ These attributes make the in-line setup particularly well-suited for studying complex dynamic systems, especially those with low absorption, where conventional absorption-based imaging techniques may struggle to provide sufficient contrast.

As depicted in Fig. 1, a shock wave propagating through the sample was generated by laser ablation at the sample surface. We used the MEC long-pulse laser ($\lambda_{\text{drive}} = 527$ nm) with a 10 ns flat-top laser pulse to deliver a total of 79.95 J of energy, generating a shockwave that interacts with the void. To image this interaction, 95 beryllium compound refractive lenses (CRLs) focused the x-rays 278 mm after the Be CRLs, with the sample positioned 63.5 mm beyond the focal point. The focal spot size in this experiment was not directly measured; however, prior studies employing similar optical configurations have reported focal spot sizes in the range of ~ 100 – 200 nm.⁴⁹ While this range suggests the potential resolution achievable with our setup, the actual resolution is ultimately limited by the system's point spread function (PSF), which we estimated to be ~ 400 nm, as discussed in Appendix D. Divergent 18 keV x-rays (0.2% bandwidth⁴⁹) from the focal point illuminated the sample, and single-shot XPC images were recorded at a distance of 4669 mm from the sample, with a $2\times$ objective lens providing a total XPC image magnification of $74.4\times$ on a Zyla detector with physical pixel size $dx = 6.5\mu\text{m}$. The optical configuration included a phase corrector, designed to manipulate the wavefront's phase profile in order to compensate for optical aberrations. Assuming the paraxial approximation⁵⁰ and using the Fresnel scaling theorem described by Paganin,⁵¹ a Fresnel diffraction pattern captured under divergent illumination can be transformed to correspond to plane wave illumination⁵² by scaling the physical detector pixel size (dx) and sample-to-detector propagation distance (z_{12}) according to the magnification factor M . Defining the magnification as $M = z_{02}/z_{01} = (z_{01} + z_{12})/z_{01}$, the effective propagation distance ($z_{\text{eff}} = z_{12}/M$) and the effective pixel size ($dx_{\text{eff}} = dx/M$) were calculated as 62.73 mm and 43.67 nm, respectively. Here, z_{01} is the source-to-sample distance, and z_{02} is the source-to-detector distance. With these scaled parameters, the Fresnel number can be converted into an effective Fresnel number, written as^{40,43}

$$Fr_{\text{eff}} = \frac{dx_{\text{eff}}^2}{z_{\text{eff}}\lambda}. \quad (2)$$

Here, dx_{eff} is the smallest characteristic feature size of the sample, corresponding to the effective pixel size, and λ is the XFEL wavelength. Small Fresnel numbers ($Fr_{\text{eff}} \ll 1$) indicate the holographic regime, while larger values ($Fr_{\text{eff}} \geq 1$) correspond to the direct-contrast (edge-enhancement) regime.^{40,43} For this study, we operate up to the holographic regime with Fr_{eff} as small as 4.41×10^{-4} , which corresponds to the smallest feature that we image in this study. This configuration enhances the ability to visualize dynamic phenomena, magnifying the features of interest. These attributes make it a powerful and versatile method for studying complex processes, such as void collapse.

XPC imaging allows visualization of the shock front, enabling a precise and direct measurement of its propagation within the sample and shock speed variations over time. For the drive conditions previously described (i.e., 10 ns flat-top drive delivering ~ 80 J), the measured shock speed (U_s) is $19.7 (\pm 0.1)$ km/s, which corresponds to a pressure of $270 (\pm 10)$ GPa according to the polyamide EOS.⁵³ Due to the initial density and shock property similarities between polyamide and SU-8, the polyamide EOS is considered to be a reasonable

surrogate for modeling SU-8 under shock loading. These conditions are crucial in understanding void-shock interactions in the high-energy-density (HED) regime, offering valuable insights into direct-drive implosion concepts using glow-discharge polymer (GDP) or polymethyl methacrylate (PMMA) ablaters. These interactions occur on timescales comparable to the onset of Rayleigh–Taylor (RT) instabilities,^{54,55} making them particularly relevant for studying implosion dynamics.

III. XPC IMAGE FORMATION

Generally, assessing the accuracy of phase retrieval algorithms would require access to the ground truth phase associated with the experimental images. However, because our sample is destroyed upon interaction with the compressive shockwave, obtaining ground truth data is not possible. Therefore, validating our experimental reconstructions necessitates the use of simulations that replicate the conditions of the experiment. To ensure a one-to-one correspondence between simulation and experimental XPC image data, we present a method that can generate realistic synthetic XPC images that account for blur, speckle, and noise that are present in our experimental XPC images. Other factors that we consider in Sec. IV include the pointing stability of the XFEL beam, the real space size of the XFEL beam, and the aperture of the Be CRL that limits the field of view (FOV) of our sample. In the following, we present our approach for simulating realistic XPC images in the holographic regime ($Fr_{\text{eff}} \ll 1$) for validation purposes. However, this can also be generalized to simulate XPC images in the direct-contrast regime ($Fr_{\text{eff}} \geq 1$). In this context, we assume the projection approximation⁵¹ and write the transmission function of our object as

$$T(x, y) = \exp([i\phi(x, y) - \mu(x, y)]), \quad (3)$$

where $\phi(x, y)$ and $\mu(x, y)$ encapsulate the phase shifting and attenuation properties of the object, respectively. Derivation of Eq. (3) can be found in Appendix A. If we denote the wavefield that illuminates our object as $\psi_0(x, y)$, the complex exit wave (EW) of the object can be expressed as

$$\psi_{EW}(x, y) = \psi_0(x, y) \cdot T(x, y), \quad (4)$$

where $\psi_0(x, y)$ contains both the illumination amplitude and phase immediately after the object, which are unknown and must be determined.⁴²

To compute the complex wavefield at the detector plane located at a distance z_{eff} , we use the Fresnel propagation transfer function (TF) kernel,⁵⁶ written as

$$H(f_x, f_y) = e^{ikz_{\text{eff}}} \exp\left(-\frac{i\pi(f_x^2 + f_y^2)}{Fr_{\text{eff}}}\right). \quad (5)$$

Here, (f_x, f_y) represent the 2D spatial frequency coordinates corresponding to (x, y) . The inclusion of Fr_{eff} accounts for the cone beam geometry used in capturing XPC images. The derivation of this equation, along with the associated sampling conditions, is provided in Appendix A.

Given Eq. (5), we can construct the Fresnel free-space propagator operator for cone beam geometry as

$$\mathcal{D}_{Fr_{\text{eff}}}[\psi_{EW}(x, y)] = \mathcal{F}^{-1}[\mathcal{F}[\psi_{EW}(x, y)] \cdot H(f_x, f_y)]. \quad (6)$$

In this expression, \mathcal{F} and \mathcal{F}^{-1} represent the Fourier transform and its inverse, respectively. Taking the squared modulus of Eq. (6) yields

$$I(x, y) = \text{Poisson}(|\mathcal{D}_{\text{Fr,eff}}[\psi_{EW}(x, y)]|^2 \otimes \text{PSF}(x, y)), \quad (7)$$

where we consider an XPC intensity image primarily contaminated with Poisson noise⁵⁷ given our experimental conditions. Additionally, for modeling, we assume that the XPC image is dark-field corrected. The point spread function, $\text{PSF}(x, y)$, is included here to encapsulate all distortions introduced by the optical system, including aberrational effects of the system, geometrical distortions caused by the scintillator, and partial coherence of the x-rays. Equation (6) consists of linear operators, but the introduction of the squared modulus and noise in Eq. (7) eliminates the possibility of a straightforward inverse transformation to recover the phase, thereby transforming the problem into a nonlinear inverse problem. Furthermore, the problem becomes under-constrained because our transmission function involves complex variables, while the detector data are real valued. Therefore, we incorporate a phase retrieval method to solve the phase problem given a single XPC image. Using Eq. (7), we will generate synthetic XPC images comparable to those captured experimentally, providing a one-to-one comparison between simulation and experiment.

IV. FORWARD MODELING AND IMAGE PREPROCESSING

To benchmark our experimental images, we simulate XPC image formation using the equations outlined in Sec. III. Similar to Leong *et al.*,³⁹ we construct a forward model for two cases: (1) a static sample, where a hollow SiO_2 void is embedded in SU-8 with no shockwave present, and (2) a dynamic sample, where the same sample undergoes shock compression. We refer to these cases as the “static” and “dynamic” images, respectively, throughout the remainder of this

manuscript. Additionally, we construct white fields for each of these cases using this forward model approach to replicate the white fields captured experimentally.

For optimal phase reconstructions, we apply preprocessing techniques—background subtraction, flat-field correction, and deconvolution—to the simulated XPC images in Subsec. IV A and the experimental images in Subsec. IV B. To ensure more consistent and accurate phase reconstructions, the exterior regions beyond the limited FOV are extended using edge values within the sample FOV.

A. Synthetic simulations and preprocessing for phase retrieval

To generate synthetic XPC images that closely resemble experimental data, several key components of the optical system must be considered for meaningful comparisons: (1) the illumination beam that interacts with the sample, (2) the influence of speckle on the CRLs, (3) the physical characteristics of the void, (4) the system’s PSF contributing to XPC image blurring, and (5) the presence of noise inherent to the imaging process. Collectively, these factors are critical as they impact the accuracy of phase reconstructions.

We begin by modeling Eq. (4) step by step, as illustrated in Figs. 2 and 3, assembling all necessary components in the z_{01} plane. Once the components are fully constructed, we apply Eq. (7) to generate the final synthetic in-line holograms. As a first step, we model $\psi_0(x, y)$ in Eq. (4) for both the static and dynamic cases, denoted as $\psi_{0,s}(x, y)$ and $\psi_{0,d}(x, y)$. Separate synthetic illumination functions are constructed to account for variations in illumination conditions, including amplitude fluctuations and pointing stability between images in these datasets. As outlined in Sec. III, the illumination amplitude and phase of $\psi_{0,s}(x, y)$ and $\psi_{0,d}(x, y)$ are unknown. In our case, the phase of the illumination beam can be approximated as a constant, since we assume that the

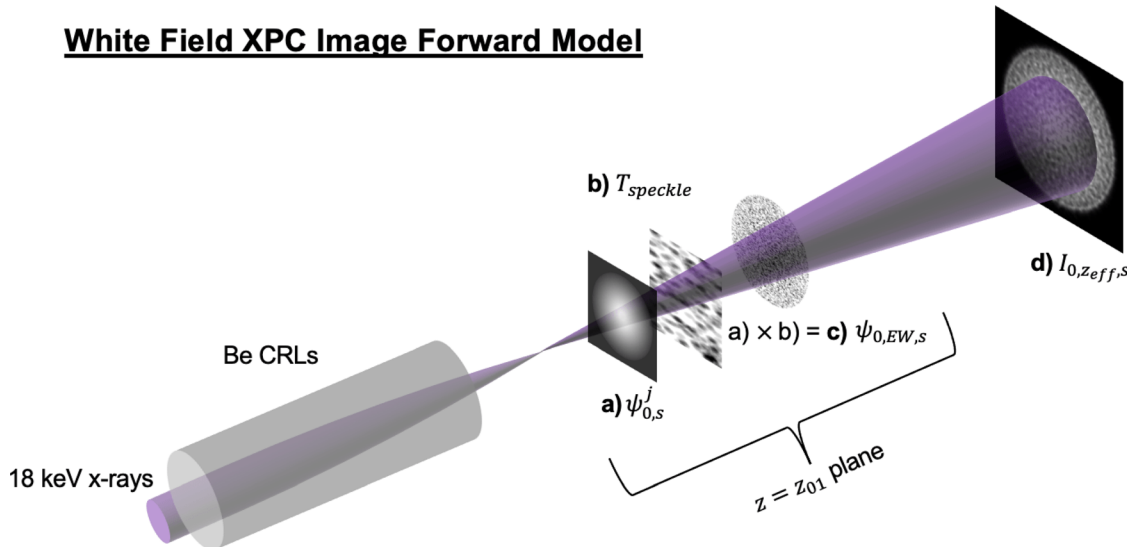


FIG. 2. White field XPC image forward model for constructing synthetic white field images that are used for flat-field correction for the synthetic static and dynamic image cases. The model was constructed in the order of (a)–(d). This model incorporates illumination beams, accounting for beam shifts, the super-Gaussian profile, and the top-hat function [Eq. (8)] shown in (a), the CRL lens speckle [Eq. (9)] shown in (b), and the exit wave [Eq. (10)] shown in (c). The exit wave is propagated using Eq. (7) to construct white fields at distance z_{eff} , shown in (d). Note: Although the schematic depicts only the static illumination case, the procedure is the same for the dynamic case. Additionally, the images for $\psi_{0,s}$, T_{speckle} , and $\psi_{EW,0,s}$ are inherently complex but are depicted as real images for illustration purposes.

Static/Dynamic XPC Image Forward Model

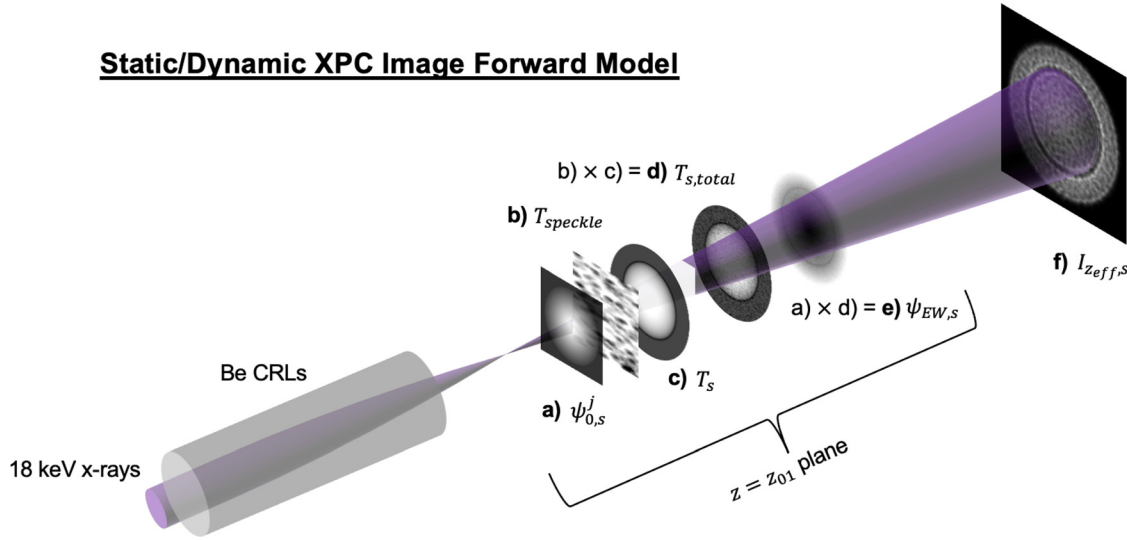


FIG. 3. Static/dynamic XPC image forward model. The model was constructed in the order of (a)–(f). This model includes the illumination beams [Eq. (8)] shown in (a), the CRL lens speckle [Eq. (9)] shown in (b), the transmission function of the sample without speckle [Eq. (11)] shown in (c), the transmission function with speckle [Eq. (14)] shown in (d), and the exit wave of sample [Eq. (15)] shown in (e). The exit wave is propagated using Eq. (7) to construct static and dynamic XPC intensity images at distance z_{eff} shown in (f). Note: Although the schematic depicts only the static sample case, the procedure is the same for the dynamic case. Additionally, the images $\psi_{0,s}^j$, T_{speckle} , T_s , $T_{s,\text{total}}$, and $\psi_{EW,s}$ are inherently complex but are depicted as real images for illustration purposes.

wavefront phase curvature varies sufficiently slowly. This results in a uniform phase offset that can be adjusted in the final stage of the phase retrieval process. Consequently, we focus mainly on the illumination amplitude and factors such as beam type, beam size, beam pointing stability, and beam fluctuations to construct and estimate $\psi_{0,s}(x, y)$ and $\psi_{0,d}(x, y)$. To avoid redundancy, we define $\psi_{0,q}(x, y)$, where $q \in s, d$ denotes either the static (s) or dynamic (d) image. With this notation, the illumination beam $\psi_0(x, y)$ in Eq. (4) can be fully expressed for the static and dynamic cases as follows:

$$\psi_{0,q}^j(x, y) = A_{0,q}^j(x, y) \cdot \psi_{0,\text{superGaussian}}(x, y) \cdot \psi_{0,\text{tophat}}(x, y). \quad (8)$$

Here, $A_{0,q}^j$ is a random variable that varies from shot to shot and takes on different peak amplitude values j , obtained from the 2D Gaussian fits described in Appendix C. The functions $\psi_{0,\text{superGaussian}}$ and $\psi_{0,\text{tophat}}$ represent the super-Gaussian and tophat profiles, respectively. Peak shifts extracted from the 2D Gaussian fits (Appendix C) were applied to $\psi_{0,\text{superGaussian}}$ to model the pointing stability of the XFEL beam. While this approach does not fully capture the slight changes in the wavefront's angle of incidence on the sample, it is sufficient for our purpose, as the primary goal was to reproduce the observed intensity fluctuations between pulses. Additional details on constructing these illumination functions can be found in Appendix C. While Eq. (8) generally represents a complex-valued illumination field with both amplitude and phase components, we assume the phase curvature varies slowly, as previously discussed. Therefore, in our implementation, we treat Eq. (8) as real-valued. However, we acknowledge that in the general case it should be considered complex, as the experimental wavefront is inherently complex. Equation (8) was used to construct synthetic illumination datasets consisting of 50 images each ($j = 50$), which is comparable to the number of white field images recorded

experimentally. The object beam illumination presented in Eq. (8) is shown in Figs. 2(a) and 3(a).

Next, we model the influence of the lens-induced speckle and the sample in the XPC image formation process using the transmission function $T(x, y)$ in Eq. (4). This function captures both the sample properties and imperfections in the CRLs that introduce speckle along the x-ray path, such as dust particles and lens defects. Since the lens-induced speckle, static sample, and dynamic sample exhibit distinct phase-shifting and absorption characteristics, we define a separate transmission function for each. We begin by defining the transmission function for the CRL speckle, written as

$$T_{\text{speckle}} = \exp([i\phi_{\text{speckle}}(x, y) - \mu_{\text{speckle}}(x, y)]), \quad (9)$$

where we assume the CRLs to be infinitely thin, such that their sole contribution to the optical system is captured by the multiplicative speckle term T_{speckle} . To model the experimental speckle (ϕ_{speckle} and μ_{speckle}), we generated a synthetic 3D vacuum-filled box filled with randomly distributed ellipsoidal SiO_2 particles, following the approach of Leong *et al.*³⁹ By projecting along the z direction of the 3D box (x-ray beam direction) we obtained 2D phase and attenuation maps (ϕ_{speckle} and μ_{speckle}) that can be inserted into Eq. (9) to give the full contribution of the CRL speckle. The speckle contribution is shown in Figs. 2(b) and 3(b). By combining Eqs. (8) and (9), we can express the total exit wave (EW) of the illumination and speckle (for generating synthetic white fields) as

$$\psi_{0,EW,q}(x, y) = \psi_{0,q}(x, y) \cdot T_{\text{speckle}}(x, y), \quad (10)$$

which fully characterizes the complex beam-speckle interaction in the z_{01} plane and is shown in Fig. 2(c). This expression captures the

combined contribution of the illumination profile and the speckle pattern introduced by the CRL at this plane.

Next, we define a transmission function to describe the contributions of the static and dynamic sample

$$T_q(x, y) = \exp([i\phi_q(x, y) - \mu_q(x, y)]). \quad (11)$$

Specifically, the 2D phase and attenuation maps (ϕ_s and μ_s) for our static sample in Eq. (11) were generated using the analytical equation of a sphere, written as

$$\begin{aligned} \phi_s = & -k \cdot \delta_{\text{SU8}} \left(t_{\text{SU8}} - \sqrt{d_{\text{out}}^2 - (x - x_c)^2 - (y - y_c)^2} \right) \\ & + \delta_{\text{SiO}_2} \left(\sqrt{d_{\text{out}}^2 - (x - x_c)^2 - (y - y_c)^2} \right. \\ & \left. - \sqrt{d_{\text{in}}^2 - (x - x_c)^2 - (y - y_c)^2} \right), \end{aligned} \quad (12)$$

and

$$\begin{aligned} \mu_s = & k \cdot \beta_{\text{SU8}} \left(t_{\text{SU8}} - \sqrt{d_{\text{out}}^2 - (x - x_c)^2 - (y - y_c)^2} \right) \\ & + \beta_{\text{SiO}_2} \left(\sqrt{d_{\text{out}}^2 - (x - x_c)^2 - (y - y_c)^2} \right. \\ & \left. - \sqrt{d_{\text{in}}^2 - (x - x_c)^2 - (y - y_c)^2} \right), \end{aligned} \quad (13)$$

which projects the sample onto a 2D plane, as shown in Fig. 3(c). Here, δ and β correspond to the real and imaginary parts of the refractive index (see Appendix A) for their respective material. The parameters x_c and y_c represent the offset coordinates of the void, d_{out} and d_{in} represent the outer and inner void diameters, respectively, and t_{SU8} is the SU-8 thickness along z . However, because of the nonlinear and complex nature of shock compression, Eqs. (12) and (13) cannot be applied to generate dynamic phase and attenuation maps. Instead, xRAGE was used to generate ϕ_d and μ_d for Eq. (11), as it accurately captures the nonlinear dynamics of the void collapse process. When constructing these simulations, we did not include material strength effects, as the melting timescale in this experiment is extremely short (sub-100 ps). This simplification is justified by the observed agreement between xRAGE simulations and experimental data.³⁸ Furthermore, the shock strength exceeds the melt thresholds for both SU-8 and SiO₂, effectively eliminating the consideration of material strength under these conditions.

The transmission functions for both the static and dynamic samples must also account for the speckle contribution, since both components lie along the same x-ray beam path, as illustrated in Figs. 3(b) and 3(c). This results in a total transmission function for both the static and dynamic cases, defined as

$$\begin{aligned} T_{q,\text{total}}(x, y) = & T_q(x, y) \cdot T_{\text{speckle}}(x, y) \\ = & \exp(i[\phi_q(x, y) + \phi_{\text{speckle}}(x, y)] \\ & - [\mu_q(x, y) + \mu_{\text{speckle}}(x, y)]), \end{aligned} \quad (14)$$

which is depicted in Fig. 3(d). By combining Eqs. (8) and (14), we can express the total EW of the static and dynamic sample in Eq. (4) as

$$\psi_{EW,q}(x, y) = \psi_{0,q}(x, y) \cdot T_{q,\text{total}}(x, y), \quad (15)$$

which fully characterizes the complex beam-speckle-sample interaction in the z_{01} plane and is shown in Fig. 3(e). This expression captures the combined contribution of the illumination profile, the transmission function of the static/dynamic object, and the speckle pattern introduced by the CRLs at this plane. The final components of the forward model to consider are the geometric parameters of the sample and the system's PSF, with details provided in Appendix D.

With all components of our forward models established, we can now construct the synthetic white field and sample XPC images. The synthetic white fields, corresponding to the experimental static and dynamic white field datasets, are obtained by applying Eqs. (7)–(10)

$$I_{0,z_{\text{eff}},q} = \text{Poisson}(|\mathcal{D}_{\text{Fr,eff}}[\psi_{0,EW,q}(x, y)]|^2 \otimes \text{PSF}(x, y)), \quad (16)$$

producing white field XPC images resembling those in Fig. 2(d). Two distinct sets of white-field images are required, as the static and dynamic XPC images were captured under different illumination conditions, with the white fields generated accordingly. Consequently, the synthetic white-field datasets are used for flat-field correction, each corresponding to its respective sample XPC image. Similarly, the static and dynamic XPC images are generated by applying Eqs. (7)–(15)

$$I_{z_{\text{eff}},q} = \text{Poisson}(|\mathcal{D}_{\text{Fr,eff}}[\psi_{EW,q}(x, y)]|^2 \otimes \text{PSF}(x, y)), \quad (17)$$

producing XPC images resembling those depicted in Fig. 3(f). Given Eqs. (16) and (17), we have fully constructed synthetic white field and sample XPC images that closely correspond to the experimental data. This can be seen by comparing Figs. 4(a) and 4(c) and Figs. 5(a) and 5(c).

To remove the dependence on ψ_0 in Eq. (4), a flat-field correction scheme is applied. Typically, this is accomplished by dividing the static/dynamic XPC images by the average of the recorded white fields, such as dividing Eq. (17) by the average of the white field images obtained from Eq. (16). However, due to the stochastic nature of the XFEL^{43,58} and the strength of refraction caused by the shockwave,⁵⁹ this approach is insufficient and more advanced methods must be applied. Therefore, we apply the FFC method described by Hodge *et al.*,³⁷ which combines image registration with principal component analysis (PCA)⁴³ to enhance visibility of features in the sample and is a critical preprocessing step prior to phase retrieval. It should be noted that image registration on its own is insufficient⁴³ and should be used together with PCA, which is the method used here.

For the image registration procedure, we utilized an image registration algorithm with the gradient descent optimizer and the ANTsNeighborhoodCorrelation⁶⁰ metric from the Python SimpleITK library.^{44,61,62} This image registration technique non-diffeomorphically warps source images using a cross-correlation-based approach to match their corresponding target images. Although the cross-correlation-based approach is an intensity-based similarity metric, it is performed over small kernels, which mitigates the effects of slow variations in the illumination. Non-diffeomorphic warping corrects both shifts and structural changes in the speckle pattern. With this technique, we aligned the white fields obtained from Eq. (16) to the first white field in their respective sets, creating new white field datasets aligned to the first white field. Then, these new white-field datasets were aligned to their corresponding sample XPC images that were computed using Eq. (17). This technique effectively reduced the influence of lens defects and artifacts in the shocked region, which arises

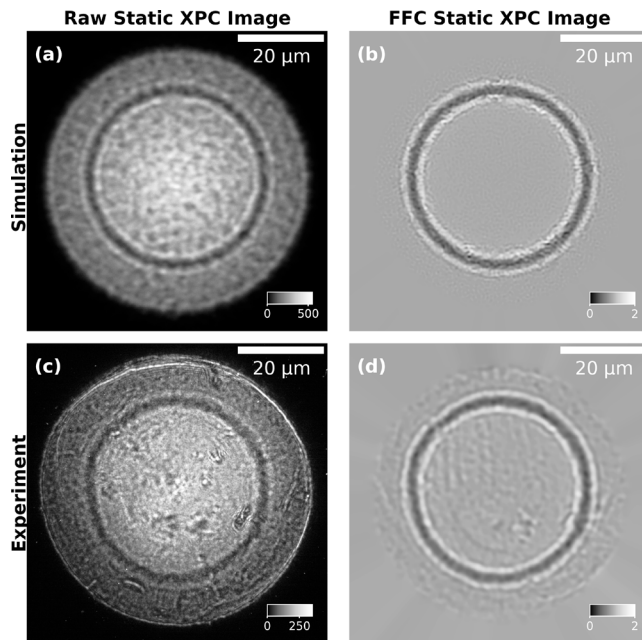


FIG. 4. Raw synthetic and experimental static XPC images and their corresponding FFC images using the combination of image registration and PCA. (a) Raw synthetic static XPC image generated from the equations in Sec. IV. (b) FFC + deconvolved image of (a) using image registration, PCA, and deconvolution with a Gaussian PSF. The exterior of the sample FOV was extended radially outward using edge values of the FOV. (c) Raw experimental static XPC image. (d) FFC + deconvolved image of (c) using image registration, PCA, and deconvolution with a Gaussian PSF. The exterior of the sample FOV was extended radially outward to the edge of the computational domain.

from the mismatch between white-field and sample XPC images due to the highly refractive shockwave as seen in Figs. 35(a) and 35(d) in Subsection 1 of the Appendix E. However, it fails to suppress low-frequency beam fluctuations, which compromises the effectiveness of flat-field correction and leads to poor phase retrieval performance. Thus, PCA is required as a secondary step, as described in Hodge *et al.*³⁷ Additional details regarding the parameters used for image registration can be found in Subsection 1 of the Appendix E.

To correct for the varying beam structure (low-frequency-beam fluctuations) in the simulated XPC images, we applied PCA to the set of white field images that had been aligned to the corresponding simulated XPC data.⁴³ For our simulations, we generated 50 white field images for both the static and dynamic cases and used the full set as input into the PCA algorithm. For the static XPC image, we found that it was best to use 20 components, accounting for >85% of the variance of the XFEL beam. For the dynamic image, we found that omitting the subtraction of E_{avg} , as originally described in the PCA flat-field correction method by Hagemann *et al.*,⁴³ led to improved phase reconstructions. Retaining the E_{avg} subtraction produced phase retrieval results that were physically inconsistent with the expected response of the material to the shockwave compression, even when one or multiple components were considered. In contrast, excluding the E_{avg} term resulted in reconstructions that aligned more closely with physical intuition. Under these conditions, using a single principal component

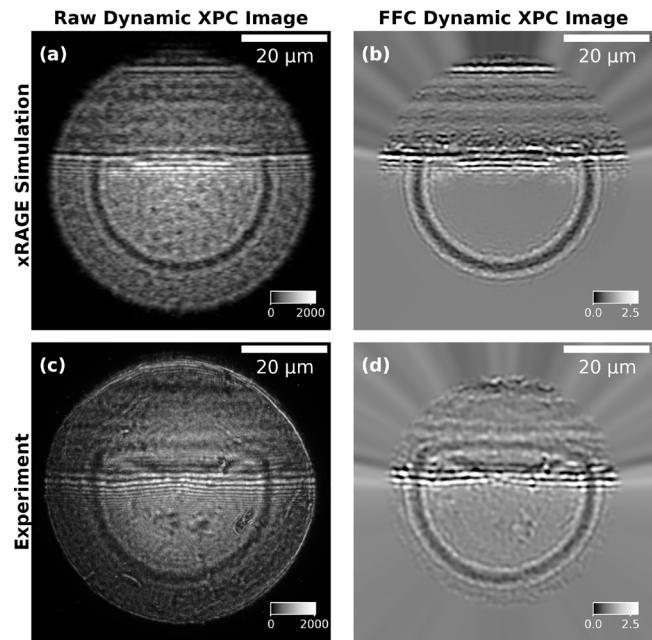


FIG. 5. Raw synthetic and experimental dynamic XPC images and their corresponding FFC images using the combination of image registration and PCA. (a) Raw synthetic dynamic XPC image generated from the equations in Sec. IV. (b) FFC + deconvolved image of (a) using image registration, PCA, and deconvolution with a Gaussian PSF. The exterior of the sample FOV was extended radially outward from the edges of the sample FOV using 1500 segments. The segments were enforced to be left/right symmetric. (c) Raw experimental dynamic XPC image. (d) FFC + deconvolved image of (c) using image registration, PCA, and deconvolution with a Gaussian PSF. The exterior of the sample FOV was extended radially outward from the edges of the sample FOV using 1500 segments. The segments were enforced to be left/right symmetric.

yielded the most accurate results, whereas including additional components degraded the quality of the FFC XPC image and its corresponding phase retrieval result. The final PCA FFC output was obtained by dividing each static and dynamic XPC image by the synthetic white field produced by the PCA algorithm, which was generated separately for each white-field dataset. This correction improved image quality and enhanced the reliability of phase retrieval.

To compensate for the blurring caused by the optical system, we deconvolved our synthetic FFC XPC static and dynamic images with the method proposed by Chan *et al.*⁶³ In our case, we used a 2D symmetric Gaussian function with its standard deviation, σ , determined by fitting an XPC simulated synthetic SiO₂ shell to that of an FFC XPC static image as described in Appendix D. After deconvolution, we extended the synthetic static and dynamic XPC images radially from the circular edge of the FOV to the boundary of the computational domain, as seen in Figs. 4(b) and 5(b). This assumption was based on the expectation that the exterior values would be extensions of those within the FOV. While the region outside the sample FOV is unknown, radially extending these values improved the convergence of the phase reconstruction within the circular FOV.⁶⁴ Without this extension, phase retrieval algorithms interpret the circular aperture's edge as a Fresnel fringe, leading to inaccuracies in object phase reconstruction. By extending the object's limited FOV, we significantly

enhanced the quality of the phase reconstructions. These synthetic FFC XPC images were then used as input for the phase retrieval algorithms in Sec. V.

B. Experimental preprocessing for phase retrieval

The experimental XPC images were obtained using the imaging configuration depicted in Fig. 1 with the XPC intensity image described by Eq. (7), which encapsulates the entire physical XPC imaging process. To remove dark current, dark-field images were collected and averaged beforehand and were subtracted from both the experimental white-field and sample XPC images. Additionally, we applied the “removeOutliers” function in the *holoTomoToolbox*⁴⁰ to the white fields and sample XPC images, improving image quality by filtering out anomalies. The resulting XPC images are shown in Figs. 4(c) and 5(c). To produce FFC XPC images, we applied the same image registration and PCA procedure used for the synthetic images in Subsec. IV A, using all 110 collected white-field images as input to the PCA algorithm. Furthermore, we extended the sample FOV for both static and dynamic images following the same method as with the synthetic images, as shown in Figs. 4(d) and 5(d). These processed images served as input for the phase retrieval algorithms in Sec. V.

V. PHASE RETRIEVAL METHOD AND RESULTS

As discussed in Sec. III, the inverse problem for a single XPC image is inherently ill-posed, meaning that a straightforward inverse transformation cannot uniquely recover the phase. This is solidified by Eq. (7), which shows that for an object that exhibits both absorption and phase, there are infinitely many combinations of $\phi(x, y)$ and $\mu(x, y)$ ($\beta(x, y)$ and $\delta(x, y)$) in $\psi_{EW}(x, y)$ that can produce the same XPC image.⁶⁵ To overcome this challenge, diversity measurement schemes, constraints, and/or approximations are necessary to constrain the problem and produce an optimal solution.

Diversity measurements are achieved through varying measurement parameters, such as varying z_{eff} ,⁶⁶ illumination wavelengths,^{67,68} illumination angle,⁶⁹ and lateral probe positions (ptychography)^{70,71} to provide redundancy to the data and suppress ambiguous and unrealistic solutions. Common constraints involve the support constraint,^{72,73} positivity constraint,^{74,75} and the single material constraint.^{42,43} Some approximations used are the linearization of the transport-of-intensity (TIE) equation^{76,77} and the transmission function,^{78–80} both of which are highly dependent on the experimental configuration and/or the physical properties of the sample.

Since our samples are dynamic, we cannot employ diversity measurements because it poses a significant challenge to capture multiple measurements of a void-collapsing sample in a single instance in time. Additionally, since we are working with an extended multi-material sample, we cannot enforce the traditional compact support constraint. To keep the phase retrieval method general for void-shock studies, we only use the positivity constraint for the case presented here.

The challenges in phase retrieval so far include lens-induced speckle, single image acquisition, the influence of the PSF, a limited sample FOV, the presence of multiple materials, and noise. An additional layer of complexity arises from the sample itself during compression, where large phase gradients (>30 radians) emerge due to the shockwave interaction. This presents a unique challenge in the high-energy-density regime that typically requires phase unwrapping techniques to achieve an accurate phase solution. Therefore, we propose

the CTF-fADMM and PGD methods to obviate the need for phase unwrapping while also providing accurate phase reconstructions. This is a major advantage over other imaging methods used for ICF studies.

A. CTF-fADMM

A major challenge in phase retrieval, as described by Eq. (7), is the nonlinear coupling of an object's amplitude and phase in forming an XPC image. While iterative phase retrieval algorithms can address this issue, they are computationally expensive, have no convergence guarantee, and struggle with reconstructing slowly varying phase profiles, leading to significant processing times.⁴² Additionally, most methods require phase unwrapping, which further increases computational complexity, particularly for large phase gradients. To address these limitations, deterministic approaches such as the CTF method are employed.^{79–83} The CTF method is advantageous because we can express the intensity (XPC image) in reciprocal space, providing a linear relationship between the intensity and the object's phase in reciprocal space.^{78,80} To establish this relationship, we consider the Fresnel diffraction integral [Eq. (6)] in vector form

$$T_{z_{eff}}(\vec{x}) = \frac{-ie^{ikz_{eff}}}{\lambda z_{eff}} \int T(\vec{x}') e^{\frac{in|\vec{x}-\vec{x}'|^2}{\lambda z_{eff}}} d\vec{x}', \quad (18)$$

where we assume the paraxial approximation.^{56,84} Here, $\vec{x} = (x\hat{x}, y\hat{y})$, $\vec{x}' = (x'\hat{x}, y'\hat{y})$, and $T(\vec{x})$ is defined as the transmission function in Eq. (3). By squaring Eq. (18) and taking the Fourier transform, we arrive at the ambiguity function⁷⁸

$$\mathcal{F}[I_{z_{eff}}(\vec{x})] = \hat{I}_{z_{eff}}(\vec{f}) = \int T\left(\vec{x} - \frac{\lambda z_{eff}\vec{f}}{2}\right) T^*\left(\vec{x} + \frac{\lambda z_{eff}\vec{f}}{2}\right) e^{-i2\pi\vec{x}\cdot\vec{f}} d\vec{x}, \quad (19)$$

where the hat indicates the Fourier transform of that variable and the asterisk denotes the complex conjugate. By Taylor expanding the transmission function in Eq. (3) to first order, we obtain

$$T(\vec{x}) = 1 - \mu(\vec{x}) + i\phi(\vec{x}), \quad (20)$$

where the value 1 represents the unmodulated part of the wavefront. Inserting Eq. (20) into Eq. (19) and simplifying yields the well-known contrast transfer function (CTF) equation:^{79–82}

$$\hat{I}_{z_{eff}}(\vec{f}) - \delta(\vec{f}) = -2 \cos\left(\frac{\pi|\vec{f}|^2}{Fr_{eff}}\right) \hat{\mu}(\vec{f}) + 2 \sin\left(\frac{\pi|\vec{f}|^2}{Fr_{eff}}\right) \hat{\phi}(\vec{f}). \quad (21)$$

This equation provides a linear approximation of the relationship between the Fourier transform of the intensity at a distance z_{eff} and the Fourier transforms of the amplitude and phase of ψ_{EW} .⁸² Although Eq. (21) was derived under the weak phase approximation, its validity extends to objects exhibiting a slowly varying phase.^{78,79} Additionally, Eq. (20) implies an additional assumption that $\mu \ll 1$. At this point, one can then simplify the right-hand side of Eq. (21) further by considering additional approximations to obtain the object phase: 1) assuming a homogeneous object or 2) assuming a pure phase object. For the first case, we define⁸⁵

$$\mu(\vec{x}) = k \frac{\beta}{\delta} \int \delta(\vec{x}, z) dz = -\frac{\beta}{\delta} \phi(\vec{x}), \quad (22)$$

indicating that the absorption is proportional to the phase by the factor β/δ . Taking the Fourier transform of Eq. (22) and replacing $\hat{\mu}(\vec{f})$ on the right-hand side of Eq. (21) yields the CTF filter

$$CTF = 2 \sin\left(\frac{\pi|\vec{f}|^2}{Fr_{eff}}\right) + 2\frac{\beta}{\delta} \cos\left(\frac{\pi|\vec{f}|^2}{Fr_{eff}}\right), \quad (23)$$

while for a pure phase object ($\beta = 0$), the cosine portion is eliminated, giving the second case. Given Eq. (23), we can simplify Eq. (21) and write

$$\mathcal{F}(I_{z_{eff}}(\vec{x}) - 1) = CTF \cdot \mathcal{F}(\phi). \quad (24)$$

We can solve for the phase by expressing Eq. (24) as a minimization problem^{40,80}

$$\arg \min_{\phi} \sum_j \frac{1}{2} \|\text{CTF}_j \cdot \mathcal{F}(\phi) - \mathcal{F}(I_j - 1)\|_2^2 + \frac{1}{2} \|\sqrt{\alpha} \cdot \mathcal{F}(\phi)\|_2^2, \quad (25)$$

where j indexes the captured images at different effective Fresnel numbers Fr_{eff} , I_j are the j preprocessed FFC XPC images, and Tikhonov regularization is applied by introducing the frequency-dependent term α , improving numerical stability. To implement this regularization, we adopt the two-level regularization scheme from Huhn *et al.*,⁸⁶ where α takes two different values, namely, α_{low} and α_{high} , which reduces noise amplification against low and high frequencies. Taking the gradient of Eq. (25) and setting it to 0 yields a closed-form solution to the CTF equation

$$\phi = \mathcal{F}^{-1} \left[\frac{\sum_j \text{CTF}_j \cdot \mathcal{F}(I_j - 1)}{\sum_j |\text{CTF}_j|^2 + \alpha} \right]. \quad (26)$$

Although CTF is successful on its own, we seek to follow the work of Huhn *et al.*⁸⁶ and incorporate phase range constraints as described in their constrained CTF (cCTF) method to produce reconstructions with higher accuracy. In their approach, both phase range constraints and the CTF are integrated and solved using the ADMM approach. Following this framework, the minimization problem can be expressed as⁸⁶

$$\phi_{k+1} = \arg \min_{\phi} \sum_j \frac{1}{2} \|\text{CTF}_j \cdot \mathcal{F}(\phi) - \mathcal{F}(I_j - 1)\|_2^2 + \frac{1}{2} \|\sqrt{\alpha} \cdot \mathcal{F}(\phi)\|_2^2 + \frac{1}{2\rho} \|\phi - \lambda_k\|_2^2, \quad (27)$$

which is the same as the minimization procedure in Eq. (25), but with an additional term to further constrain and simplify the problem. Solving this minimization problem yields a closed-form solution

$$\phi_{k+1} = \mathcal{F}^{-1} \left[\frac{\frac{\mathcal{F}(\lambda_k)}{\rho} + \sum_j \text{CTF}_j \cdot \mathcal{F}(I_j - 1)}{\frac{1}{\rho} + \sum_j |\text{CTF}_j|^2 + \alpha} \right], \quad (28)$$

with auxiliary variables defined as

$$\tau_{k+1} = P_C(\phi_{k+1} + \lambda_k), \quad (29)$$

and

$$\lambda_{k+1} = \lambda_k + \phi_{k+1} - \tau_{k+1}. \quad (30)$$

Thus, with phase limit constraints, solving this problem requires an iterative procedure for updating ϕ , while in the CTF minimization, only a single step is required. Here, λ_k and ϕ_k are initialized with zeros, $\rho > 0$ is a step size parameter, and P_C enforces the phase range constraints. To speed up convergence, an accelerated variant of ADMM is used and is denoted as fADMM.^{86,87} Overall, the CTF-fADMM method is beneficial since it can reconstruct slowly varying phase features, where iterative algorithms struggle or require many iterations. However, the disadvantages associated with this method include failure of reconstructing sharp edges accurately, requiring a supplemental phase retrieval method for further refinement. In Subsecs. V A 1 and V A 2, we present phase reconstructions using the CTF-fADMM method using Eqs. (27)–(30).

1. CTF-fADMM phase results: Static void

For the synthetic and experimental static sample case [see Figs. 4(b) and 4(d)], we set $\alpha_{low} = 0$ for the low-frequency regularization and $\alpha_{high} = 1.0$ for the high-frequency regularization. Additionally, we assumed a pure phase object ($\beta = 0$) since $\beta \ll \delta$, defining the CTF solely in terms of sine in Eq. (28) within the CTF-fADMM method. The algorithm was set to run for a maximum of 100 iterations or until the residual or primal (original optimization problem), as defined by Goldstein *et al.*,⁸⁷ dropped below 10^{-3} , whichever occurred first. The phase bounds were set to a range of -3 to 3 , given prior knowledge of the phase range of a SiO_2 shell embedded in SU-8, and the ρ parameter was set to 5×10^{-5} . In every iteration, we use a circular phase mask slightly smaller than the sample FOV to set the phase outside the mask to a constant value corresponding to the average of the sample FOV edges. After the reconstruction process, we subtracted a constant phase value from the entire image such that the phase range was on the same scale as the synthetic ground truth phase range. The resulting phase maps are shown in Figs. 6(b) and 6(d), sharing a close resemblance to the synthetic ground truth in Fig. 6(a).

To see the reconstruction accuracy in more detail, we can examine Figs. 7 and 8, where vertical and horizontal lineouts (denoted in blue and red) are plotted against the synthetic ground truth phase (shown in black). We determine that the SiO_2 void itself is well reconstructed, while the void shell is blurred and not as accurate. This occurs in response to the shell violating the slowly varying phase approximation as required by the CTF method. However, these outputs provide strong initial estimates for further phase refinement using the PGD method.

2. CTF-fADMM phase results: Dynamic shocked void

For the dynamic sample case [see Figs. 5(b) and 5(d)], the procedure followed exactly the same as in the static case except that the phase bounds were set to a range of -15 (maximum) to -75 (minimum), with the minimum set to be ~ 10 radians lower than what is expected from xRAGE. The parameter ρ was set to 1×10^{-5} for both the synthetic and experimental XPC images. In each iteration, we extended the phase horizontally using a phase mask slightly smaller than the FOV of the sample. This step was crucial in achieving more accurate phase reconstructions inside the sample FOV. As can be seen

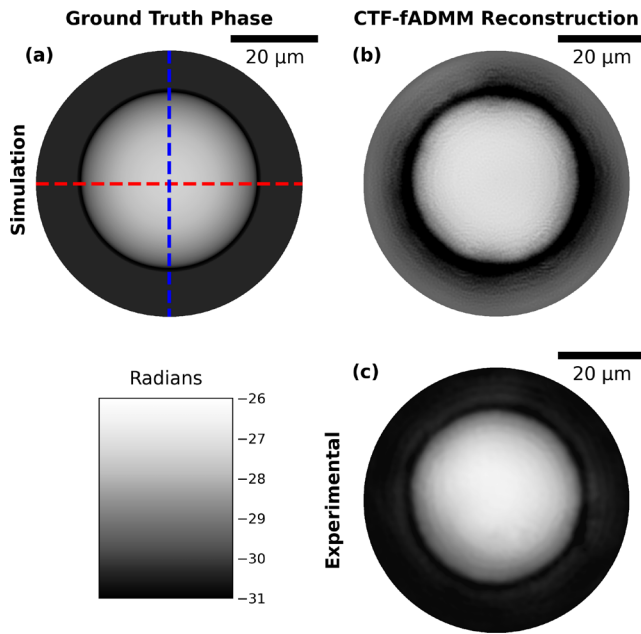


FIG. 6. Comparisons between the 2D ground truth phase and the associated CTF-fADMM reconstructions of the synthetic XPC static image and experimental XPC static image. The blue and red dashed lines correspond to the lineouts in Figs. 7 and 8. (a) Ground truth phase generated using Eq. (12). (b) CTF-fADMM phase reconstruction of the synthetic XPC static image produced as described in Sec. IV. (c) CTF-fADMM phase reconstruction of the experimental XPC static image. Note: The outputs in (b) and (c) are not the final results. Instead, (b) and (c) are initial seeds for the PGD algorithm in Sec. VB.

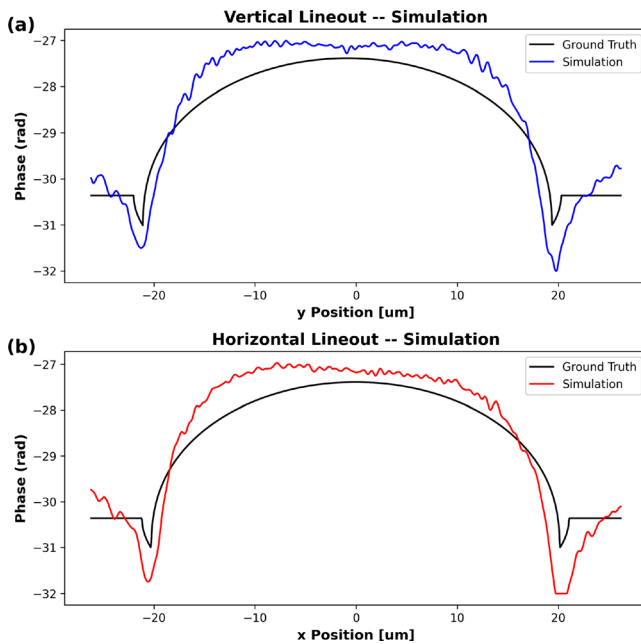


FIG. 7. (a) Vertical (blue) and (b) horizontal (red) lineout comparisons between the simulated CTF-fADMM static phase reconstructions and the ground truth phase (black).

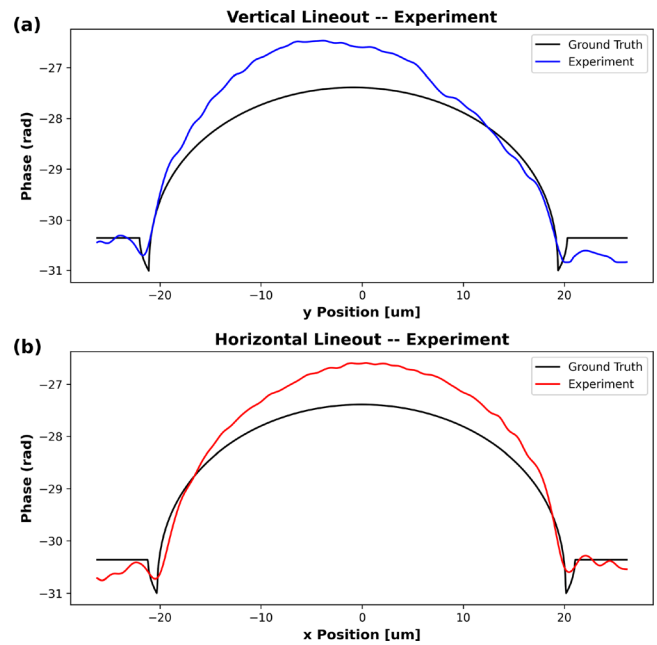


FIG. 8. (a) Vertical (blue) and (b) horizontal (red) lineout comparisons between the experimental CTF-fADMM static phase reconstructions and the ground truth phase (black).

in Figs. 9(b) and 9(c), the large shock region and the void were well reconstructed since they are slowly varying. However, the shock front and the void shell were significantly blurred in comparison to Fig. 9(a), requiring an iterative refinement procedure to capture additional void-shock details.

To visualize the sample structure from Fig. 9, we plot lineouts associated with Figs. 9(b) and 9(c) in both the vertical (blue) and horizontal (red) directions and compare them against the ground truth lineouts (black). These plots highlight the limitations of the CTF-fADMM method, particularly in regions with sharp features. While the method effectively reconstructs slowly varying phase structures fairly accurately, it struggles with abrupt changes, often leading to phase overshooting in several areas.

B. Projected gradient descent (PGD)

The CTF-fADMM gives us a strong initial approximation of the EW phase; however, we implement PGD⁴² as a method to refine and improve the phase reconstructions. The PGD method introduced by Dora *et al.*⁴² is a single-image phase reconstruction algorithm that employs downsampling, absorption regularization, and suppresses high spatial frequencies to encourage reconstruction of low spatial frequency regions. Although PGD is a powerful technique designed to reconstruct single-shot images, even for objects with large phase gradients as demonstrated in their manuscript, there is still no formal global convergence guarantee and it involves several tuning parameters that can significantly impact both the reconstruction quality and convergence time. In their implementation, the algorithm is initialized with a zero phase, which appears to work well in their specific cases (and possibly many other cases). In our application, however, we

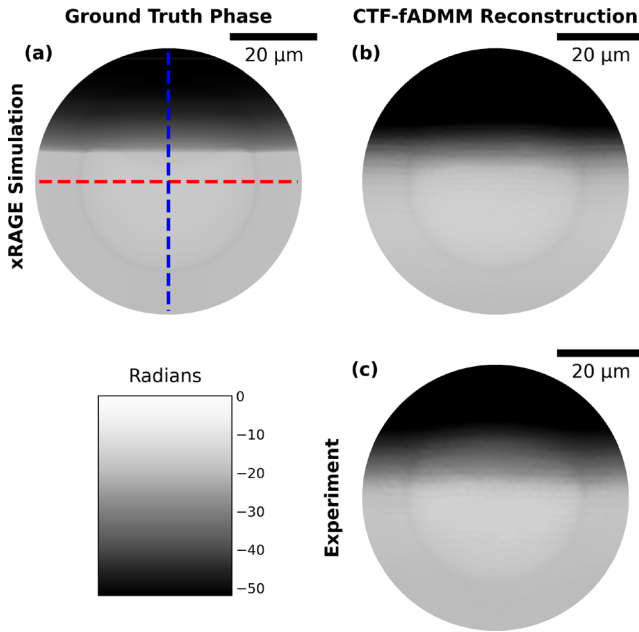


FIG. 9. Comparisons between the 2D ground truth phase and the associated CTF-fADMM reconstructions of the synthetic XPC dynamic image and experimental XPC dynamic image. The blue and red dashed lines correspond to the lineouts in Figs. 10 and 11. (a) Ground truth phase generated using xRAGE. (b) CTF-fADMM phase reconstruction of the synthetic XPC dynamic image. (c) CTF-fADMM phase reconstruction of the experimental XPC dynamic image. Note: The outputs in (b) and (c) are not the final results. Instead, (b) and (c) are initial seeds for the PGD algorithm in Sec. VB.

found that seeding the algorithm with a more informed initial phase guess led to both faster convergence and improved reconstruction accuracy. A good initial estimate not only reduces the need for extensive parameter tuning but also provides a useful baseline—if the reconstruction deviates significantly from the initial guess, it becomes easier to diagnose which parameters require adjustment. Using their approach, the goal is to minimize the following objective function:⁴²

$$S^\dagger \left[\arg \min_{\tilde{O}} \frac{1}{2} \|\mathcal{D}_{\text{Fref}}(\exp(i\tilde{O})) - \sqrt{S_\dagger} I_{\text{detector}}\|_2^2 + \chi_\Omega(\tilde{O}) + \beta \|\text{Im}(\tilde{O})\|_2 \right]. \quad (31)$$

Unlike traditional methods that reconstruct the EW of the sample, their formulation directly retrieves the complex refractive object, eliminating the need for phase unwrapping. Here, S^\dagger and S_\dagger are the upsampling and downsampling operators, respectively, while \tilde{O} represents the refractive object, equivalent to the transmission function T without the imaginary unit i outside the integral in Eq. (A5). The regularization parameter β controls the damping strength of the absorption values (if we consider both absorption and phase), ensuring stable reconstructions, and χ_Ω is the indicator function. Similar to other optimization problems, solving this minimization problem involves gradient descent with step size η . To accelerate convergence and avoid local minima,

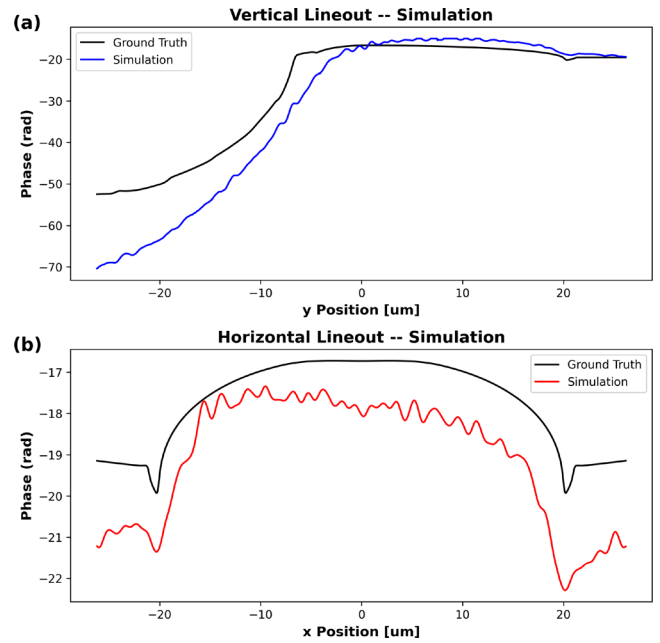


FIG. 10. (a) Vertical (blue) and (b) horizontal (red) lineout comparisons between the simulated CTF-fADMM dynamic phase reconstructions and the ground truth phase (black). Note: The scale for the vertical lineouts is much larger than the horizontal ones due to the presence of the shockwave, causing a large phase gradient compared to the unshocked void.

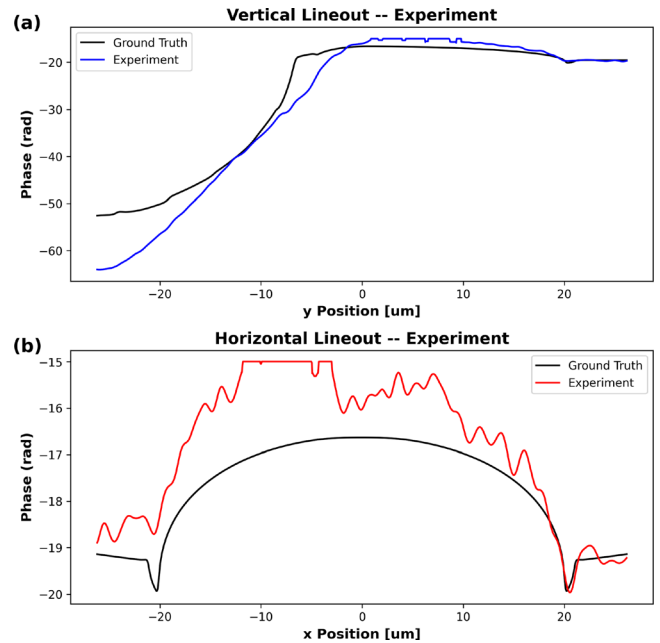


FIG. 11. (a) Vertical (blue) and (b) horizontal (red) lineout comparisons between the experimental CTF-fADMM dynamic phase reconstructions and the ground truth phase (black). Note: The scale for the vertical lineouts is much larger than the horizontal ones due to the presence of the shockwave, causing a large phase gradient compared to the unshocked void.

the method incorporates Nesterov's accelerated gradient (NAG) with parameter γ , facilitating more efficient and optimal solutions.

We do not begin with this algorithm because utilizing CTF-fADMM is a fast and computationally efficient method to recover slowly varying phase features and can be applied since approximations regarding the sample are met. Therefore, seeding this algorithm with the phase result from the CTF-fADMM method and having this algorithm refine the sharper features yielded the best results.

1. PGD phase results: Static void

To enhance the sharp features in the phase reconstructions of the CTF-fADMM method, we used its phase results from Sec. V A 1 as the initial seed for the static reconstructions in the PGD algorithm. Initially, the synthetic and experimental XPC images, along with the CTF-fADMM phase results, were downsampled by a factor of 4. The reconstruction process involved three upsampling stages: the first two stages applied an upsampling factor of 2, while the final stage retained the original resolution (upsampling factor set to 1). The phase range was set between -32 (minimum) and -26 (maximum). Additionally, at each iteration, phase values outside the sample FOV were constrained to a constant using the same phase mask as used in the CTF-fADMM method, determined by the object FOV edge values at that iteration. Additional reconstruction parameters are provided in Table I.

With these parameters, we obtained our final phase reconstructions for the synthetic and experimental static XPC images shown in Fig. 12. Figure 12(a) is the synthetic ground truth phase generated from Eq. (12) and is used as a benchmark for Figs. 12(b) and 12(c).

TABLE I. Parameters used in the PGD algorithm to reconstruct the synthetic and experimental XPC static images. The reconstruction parameters are the same for both cases. The upsampling parameter S^\dagger is part of a multigrid strategy where the optimization is performed progressively from coarse to fine grids. In this case, it upsamples twice by a factor of 2, and the final stage is the finest resolution. Nesterov's momentum governs how much of the previous gradient is carried into the current iteration in the Nesterov-accelerated gradient descent. Higher values can speed up convergence but risk overshooting and instability. η is the learning rate in the gradient descent optimization. β is the L2 regularization value, which is applied only to the imaginary part (absorption) of the complex refractive index. This stabilizes reconstructions where high absorption can otherwise destabilize the phase (real part) recovery due to numerical coupling in the forward model. The ϕ and μ smoothing occurs before applying the gradient step, which suppresses noise and promotes spatial smoothness. σ_{Fourier} (listed as σ in the manuscript by Dora *et al.*⁴²) is used to construct a Gaussian weighting function in Fourier space to dampen high spatial frequencies in the gradient update. This helps reduce overshooting artifacts and improves stability for reconstructions involving fine details. A description of these parameters can be found in the work of Dora *et al.*⁴²

Parameters	Stage 1	Stage 2	Stage 3
Iterations	500	700	2500
Upsampling (S^\dagger)	2	2	1
Nesterov's momentum (γ)	1.0	1.0	1.0
Update rate (η)	1.1	1.1	1.2
L_2 weight (β)	0	0	0
ϕ smoothing (σ_ϕ)	3.0	3.0	2.0
μ smoothing (σ_μ)	1.0	1.0	2.0
Fourier smoothing (σ_{Fourier})	200	200	0

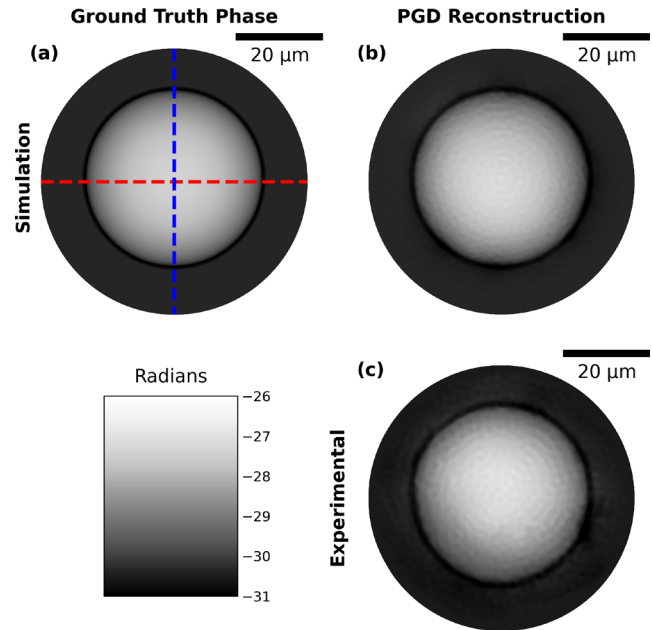


FIG. 12. Comparisons between the 2D ground truth phase and the associated PGD reconstructions of the synthetic XPC static image and experimental XPC static image. The blue and red dashed lines correspond to the lineouts in Figs. 13 and 14. (a) Ground truth phase generated using Eq. (12). (b) PGD phase reconstruction of the synthetic XPC static image using the synthetic CTF-fADMM phase reconstruction as a seed. (c) PGD phase reconstruction of the experimental XPC static image using the experimental CTF-fADMM phase reconstruction as a seed. Note: These are the final phase reconstructions, which used the initial phase results from the CTF-fADMM method in Sec. V A.

Vertical and horizontal lineouts for the synthetic and experimental phase reconstructions are shown in Figs. 13 and 14, respectively. These figures indicate that PGD produces a sharper and more accurate result than CTF-fADMM when compared to the synthetic ground truth in Fig. 12(a).

To display the accuracy of the reconstructions we plot the mean squared error (MSE) loss over the iteration number for the PGD method, which is shown in Fig. 15. The MSE is defined as $1/N \cdot \|\sqrt{I_{\text{prop}}} - \sqrt{I_{\text{detector}}}\|_2^2$, where N is the number of pixels, I_{prop} is the forward propagated and updated hologram based on the algorithm constraints, and I_{detector} is the measured experimental or synthetic hologram. These plots demonstrate that downsampling preserved the slowly varying features with minimal alteration to the object, and that the final refinement stage effectively improved the phase reconstructions, achieving errors as low as 10^{-11} and 10^{-12} for the experimental and simulated cases, respectively. Despite these low error values, discrepancies remain along the void shell, primarily due to the blurring effect of the PSF, which suppresses high-frequency features and diminishes the reconstruction fidelity. Although deconvolution was used to mitigate this effect, the presence of noise hinders ideal phase recovery. Nevertheless, the reconstructed images can still be interpreted as blurred approximations of the ground truth: they remain quantitatively accurate in regions with low spatial gradients, and while high-gradient features are less precisely recovered, the overall morphology of the shell is well preserved.

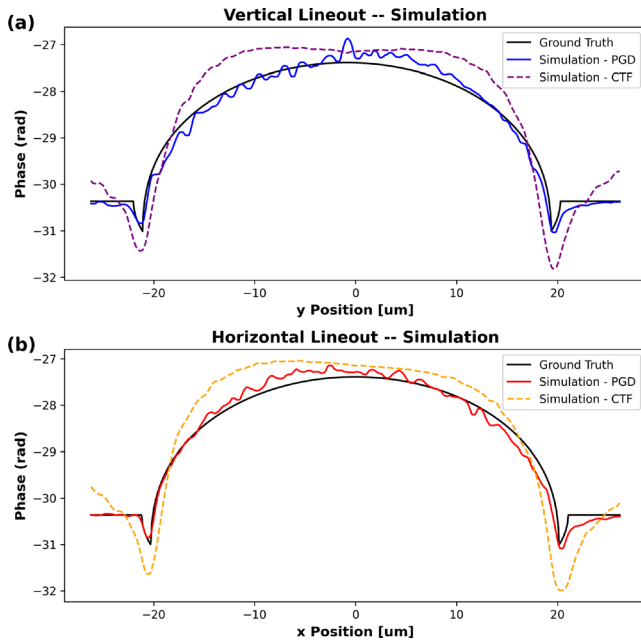


FIG. 13. (a) Vertical (blue) and (b) horizontal (red) lineout comparisons between the simulated PGD static phase reconstructions and the ground truth phase (black). The improved quality of the synthetic static reconstructions can be seen by comparing the PGD lineouts (solid blue and red lines) to the dashed purple and orange lines, which correspond to the CTF-fADMM method in Sec. VA 1.

To assess the spatial performance of the proposed CTF-fADMM and CTF-fADMM+PGD algorithms, we generated two-dimensional maps of the normalized root mean square error (NRMSE) and structural similarity index measure (SSIM), following the approach used by Leong *et al.*³⁹ These maps, shown in Fig. 16 for the simulated static images, highlight the regions where each algorithm performs well or exhibits limitations. This technique can only be applied to the simulated case since the experimental images have no associated ground truth. In the NRMSE maps, higher errors are represented by white and lower errors by black. In contrast, the SSIM maps range from 0 to 1, with a value of 1.0 indicating perfect structural agreement between the reconstruction and ground truth, and lower values reflecting reduced similarity.

2. PGD phase results: Dynamic shocked void

Similar to the PGD static reconstruction, we used the CTF-fADMM phase results in Sec. VA 2 as the initial seed for the dynamic reconstructions for the PGD algorithm. Moreover, we downsample the dynamic XPC phase and intensity images by a factor of 4. Similar to the static method, we utilized three reconstruction stages as shown in Table II. The phase range was set to -75 (minimum) to -15 (maximum) for stages 1 and 2. In stage 3, the phase range was set to -75 (minimum) to -15 (maximum), and in the last 500 iterations we altered the phase range to be -75 (minimum) to 0 (maximum). Furthermore, at each iteration, a phase mask smaller than the object FOV was used to extend the phase horizontally. Additional reconstruction parameters are provided in Table II.

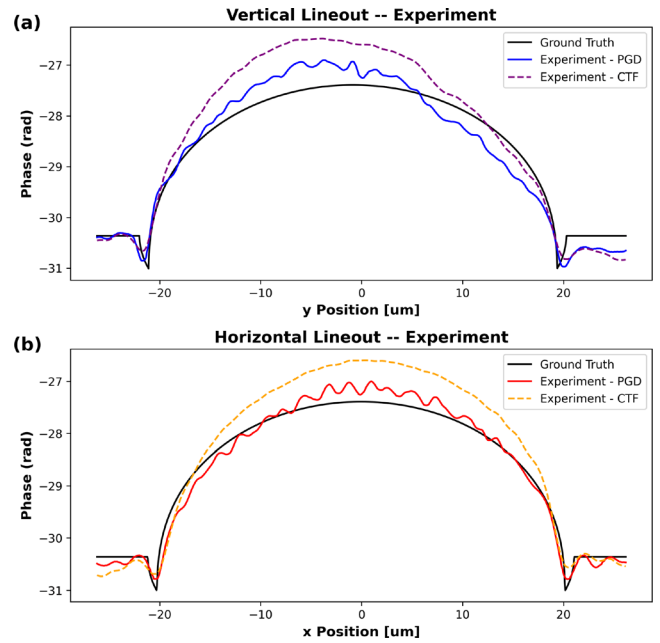


FIG. 14. (a) Vertical (blue) and (b) horizontal (red) lineout comparisons between the experimental PGD static phase reconstructions and the ground truth phase (black). The improved quality of the experimental static reconstructions can be seen by comparing the PGD lineouts (solid blue and red lines) to the dashed purple and orange lines, which correspond to the CTF-fADMM method in Sec. VA 1.

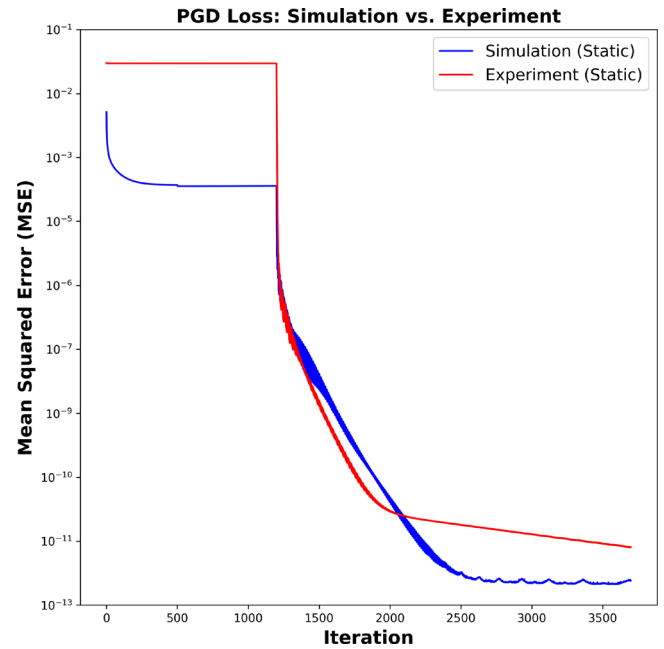


FIG. 15. Mean squared error (MSE) loss (i.e., $1/N \cdot \|\sqrt{I_{prop}} - \sqrt{I_{detector}}\|_2$) corresponding to the simulated (blue) and experimental (red) static reconstructions.

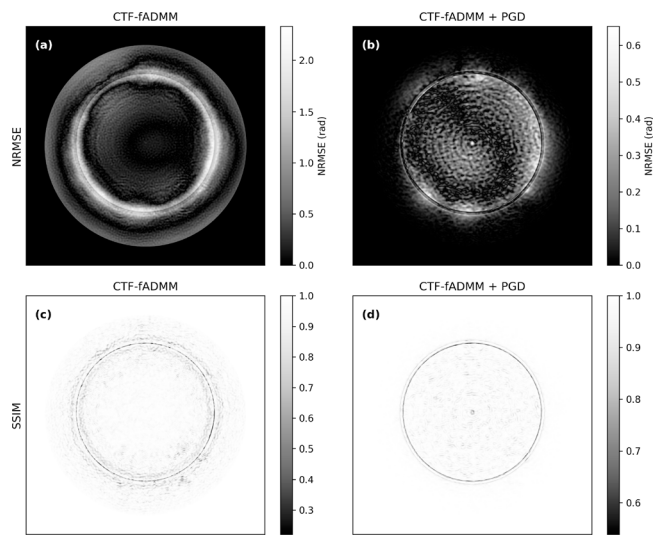


FIG. 16. Two-dimensional error and similarity maps for the static simulated reconstructions. The process of obtaining these maps is discussed in the manuscript by Leong *et al.*³⁹ Top row (a) and (b): normalized root mean square error (NRMSE) between the reconstructed and ground truth phase maps. Black indicates regions of lower error, while white indicates higher error. Bottom row (c) and (d): structural similarity index measure (SSIM), where a value of 1.0 indicates perfect structural agreement with the ground truth and lower values indicate reduced similarity. Left column (a) and (c): results from the CTF-fADMM algorithm. Right column (b) and (d): results from the combined CTF-fADMM + PGD algorithm.

TABLE II. This table lists the parameters used in the PGD algorithm to reconstruct the synthetic and experimental XPC dynamic images. The reconstruction parameters are the same between the simulated and experimental reconstructions except for the values shown in the parentheses, which correspond to the experimental reconstruction. A description of these parameters can be found in Table I and in the work of Dora *et al.*⁴²

Parameters	Stage 1	Stage 2	Stage 3
Iterations	500	500	800
Upsampling (S^\dagger)	2	1	1
Nesterov's momentum (γ)	1.0	1.0	1.0
Update rate (η)	1.1	1.1	1.1
L_2 weight (β)	0	0	0
ϕ smoothing (σ_ϕ)	2.0	3.0 (4.0)	3.0 (4.0)
μ smoothing (σ_μ)	0	0	0
Fourier smoothing (σ_{Fourier})	94	80 (58)	0

Using the parameters specified in the tables, we obtained the final phase reconstructions for the synthetic and experimental dynamic XPC images, as shown in Fig. 17. The phase map in Fig. 17(a) presents the ground truth phase generated by xRAGE, serving as a benchmark for the reconstructions in Figs. 17(b) and 17(c). To evaluate the accuracy of these reconstructions, vertical and horizontal lineouts are provided in Figs. 18 and 19. The results demonstrate that the PGD method preserves the slowly varying phase features while producing sharper details in regions near the shock front and the shell itself,

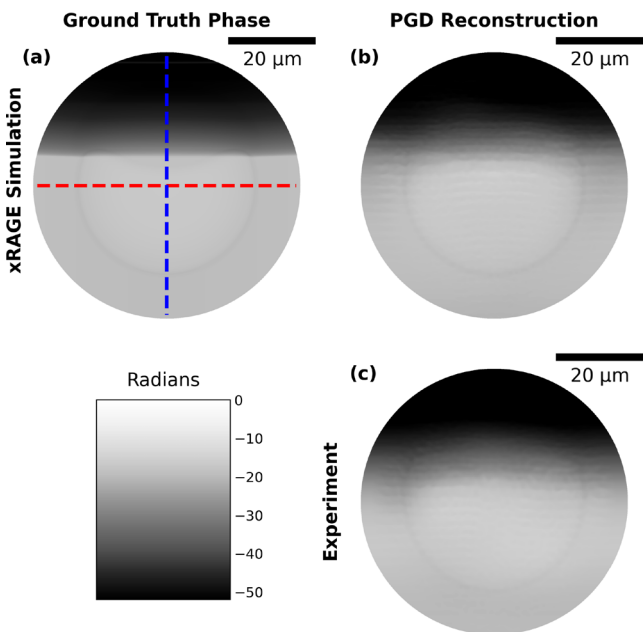


FIG. 17. Comparisons between the 2D ground truth phase and the associated PGD reconstructions of the synthetic XPC dynamic image and experimental XPC dynamic image. The blue and red dashed lines correspond to the lineouts in Figs. 18 and 19. (a) Ground truth phase generated using xRAGE. (b) PGD phase reconstruction of the synthetic XPC dynamic image using the synthetic CTF-fADMM phase reconstruction as a seed. (c) PGD phase reconstruction of the experimental XPC dynamic image using the experimental CTF-fADMM phase reconstruction as a seed. Note: These are the final phase reconstructions that used the initial phase results from the CTF-fADMM method in Sec. VA.

offering improved fidelity compared to the synthetic ground truth in Fig. 17(a). The resulting MSE loss for our synthetic and experimental dynamic reconstructions is shown in Fig. 20, with final errors reaching as low as 10^{-9} and 10^{-10} for the experimental and simulated images, respectively. While these low error values indicate a successful reconstruction, local discrepancies remain—particularly along the shock front. This is due to the influence of the PSF, which blurs high-frequency features and limits the fidelity of sharp gradients. Although deconvolution was applied to mitigate this effect, residual noise continues to constrain the accuracy of phase retrieval in these regions. As in the static case, the reconstructed images can be interpreted as smoothed representations of the ground truth: they remain quantitatively accurate in low-gradient areas, and although fine-scale features near sharp transitions are less precisely resolved, the overall structure and dynamics of the shock and jetting are well captured.

To evaluate the spatial accuracy of the dynamic reconstructions, we also generated NRMSE and SSIM maps for the simulated dynamic images,³⁹ as shown in Fig. 21. As with the static case, this analysis is restricted to simulations, since no ground truth exists for the experimental data and the reconstructed phase may deviate significantly from what is predicted by xRAGE. In the NRMSE maps, white denotes regions of higher error and black denotes regions of lower error. Similarly, the SSIM maps quantify local structural similarity, with values ranging from 0 to 1.0, where 1.0 indicates perfect correspondence

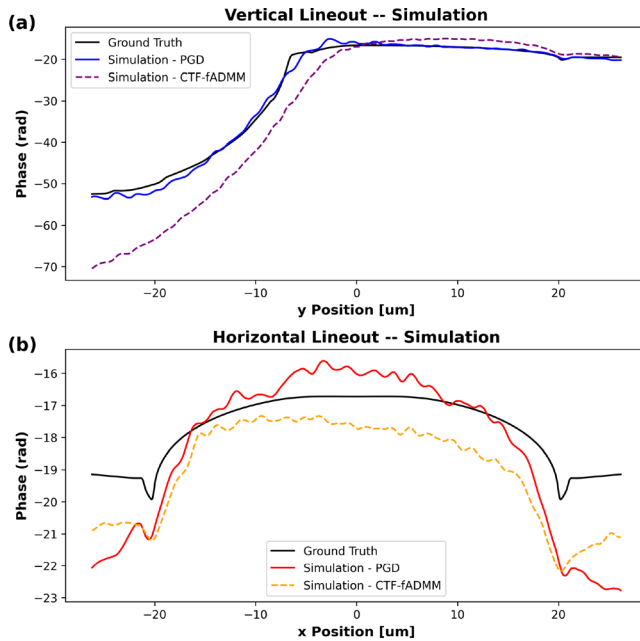


FIG. 18. (a) Vertical (blue) and (b) horizontal (red) lineout comparisons between the simulated PGD dynamic phase reconstructions and the ground truth phase (black). The improved quality of the synthetic dynamic reconstructions can be seen by comparing the PGD lineouts (solid blue and red lines) to the dashed purple and orange lines, which correspond to the CTF-fADMM method in Sec. VA2. Note: The scale for the vertical lineouts is much larger than the horizontal ones due to the presence of the shockwave, causing a large phase gradient compared to the unshocked void.

between the reconstruction and the ground truth, and lower values denote decreased similarity.

Python was used to run all the phase reconstruction algorithms described in this manuscript. Reconstructions using the CTF-fADMM algorithm were performed on a MacBook Pro with a 2.3 GHz Quad-Core Intel Core i7 processor, 16 GB 3733 MHz LPDDR4X memory, and integrated Intel Iris Plus Graphics (1536 MB). The typical reconstruction time for this method was ~ 2.5 min. Reconstructions using the PGD method were run on the Brigham Young University (BYU) Fulton Supercomputing cluster (fsl.byu.edu), utilizing a single node with one CPU core and an NVIDIA Tesla P100 GPU with 16 GB of memory. The typical reconstruction time for this method was ~ 5 min.

VI. CONCLUSION

Through analysis, such as phase retrieval via CTF-fADMM and PGD, we have successfully reconstructed a complex, multi-material sample from a single-shot measurement, capturing the nonlinear interactions between a shockwave and a void with high fidelity. Developing a forward model with xRAGE simulations to closely match the experimental data was crucial for evaluating the accuracy of the proposed phase retrieval algorithms for this dataset. While our approach relies on a CTF-based approach combined with PGD, alternative methods, such as phase retrieval initialized using the transport of intensity equation (TIE) or its variants,^{88–90} may be more suitable in experimental configurations with reduced coherence. Using this forward model as a

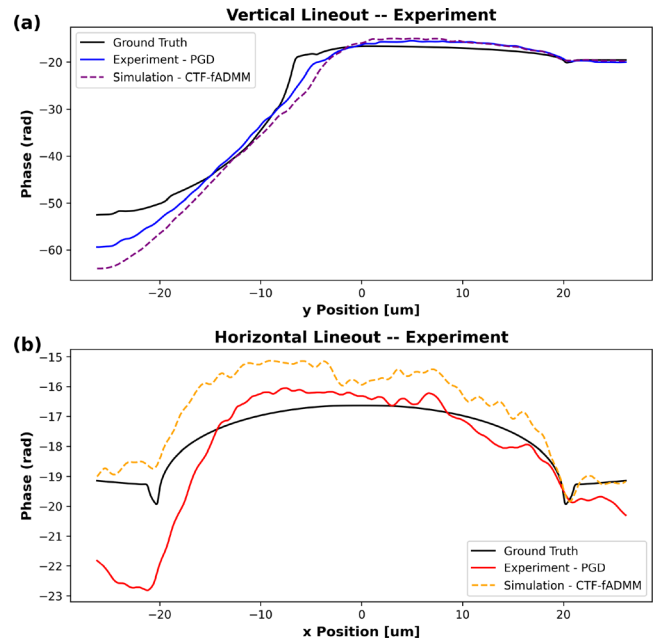


FIG. 19. (a) Vertical (blue) and (b) horizontal (red) lineout comparisons between the experimental PGD dynamic phase reconstructions and the ground truth phase (black). The improved quality of the experimental dynamic reconstructions can be seen by comparing the PGD lineouts (solid blue and red lines) to the dashed purple and orange lines, which correspond to the CTF-fADMM method in Sec. VA2. Note: The scale for the vertical lineouts is much larger than the horizontal ones due to the presence of the shockwave, causing a large phase gradient compared to the unshocked void.

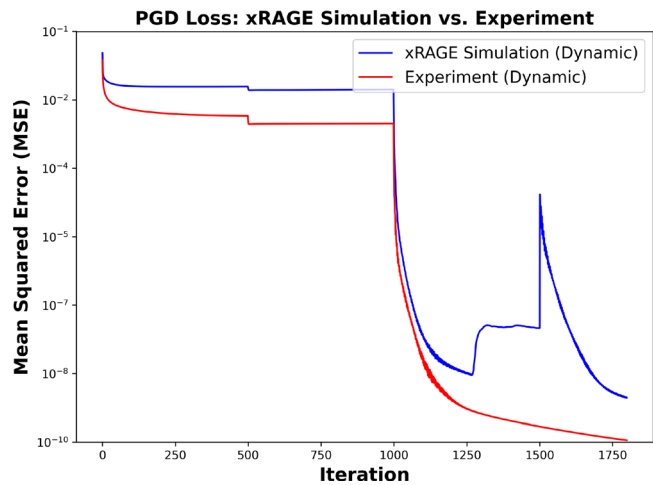


FIG. 20. Mean squared error (MSE) (i.e., $1/N \cdot \|\sqrt{I_{prop}} - \sqrt{I_{detector}}\|_2$) loss corresponding to the simulated (blue) and experimental (red) dynamic reconstructions.

benchmark, our results provide key insights into how ablator defects evolve under shock compression at various collapse stages—an essential step toward advancing inertial fusion energy (IFE) science and the feasibility of ICF-based power plants. Although the results provided

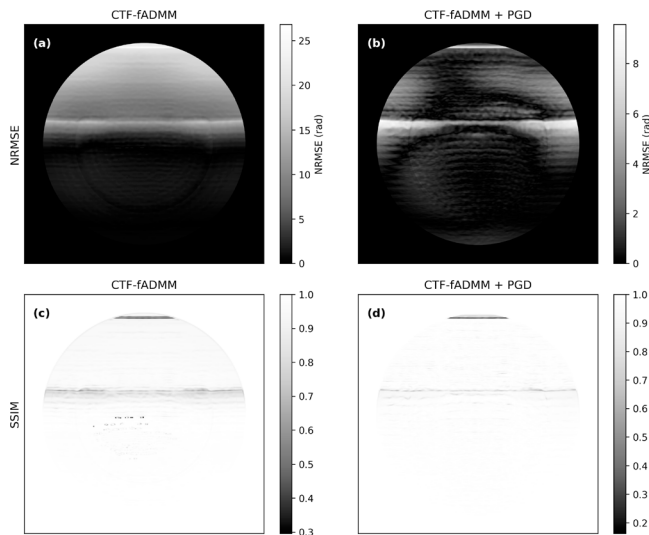


FIG. 21. Two-dimensional error and similarity maps for the dynamic simulated reconstructions. The process of obtaining these maps is discussed in the manuscript by Leong *et al.*³⁹ Top row (a) and (b): normalized root mean square error (NRMSE) between the reconstructed and ground truth phase maps. Black indicates regions of lower error, while white indicates higher error. Bottom row (c) and (d): structural similarity index measure (SSIM), where a value of 1.0 indicates perfect structural agreement with the ground truth and lower values indicate reduced similarity. Left column (a) and (c): results from the CTF-fADMM algorithm. Right column (b) and (d): results from the combined CTF-fADMM + PGD algorithm.

here are for voids larger than those in real ICF experiments, future work could further refine this understanding by investigating the interactions of smaller or multiple voids (such as foam-like materials) under ICF-relevant conditions, as even small defects can impact energy yield. Studying smaller-scale features is particularly important, as they may play an even greater role in the microphysics of collapse and directly affect plasma confinement time, a critical factor for the success of future ICF-based power plants.

ACKNOWLEDGMENTS

Funding from Office of Science, Fusion Energy Sciences (Award No. DE-SC0024882), IFE-STAR issued as SLAC FWP 101126 through the IFE RISE Hub partnership. Use of the Linac Coherent Light Source (LCLS), SLAC National Accelerator Laboratory, is supported by the U.S. Department of Energy, Office of Science, Office of Basic Energy Sciences (Grant No. DE-AC02-76SF00515). DSH, SP, AEG, and RLS acknowledge the funding support from DOE ECA-Gleason 2019. Part of this work was performed at the Stanford Nano Shared Facilities (SNSF), supported by the National Science Foundation (Grant No. ECCS-2026822). JS, HA, and KK-O acknowledge the funding support from U.S. NNSA (Grant Nos. DE-NA0003914 and DE-NA0004134) and NSF (Grant Nos. PHY-2020249, DE-SC0020229, and DE-SC0019329). AFTL acknowledges the funding support from the Laboratory Directed Research and Development (Grant No. 20200744PRD1) and Los Alamos National Laboratory (iHMX, Conventional High Explosives Grand Challenge).

AUTHOR DECLARATIONS

Conflict of Interest

The authors have no conflicts to disclose.

Author Contributions

D. S. Hodge: Conceptualization (equal); Data curation (equal); Formal analysis (equal); Investigation (equal); Methodology (equal); Software (equal); Validation (equal); Visualization (equal); Writing – original draft (equal); Writing – review & editing (equal). **A. F. T. Leong:** Data curation (equal); Formal analysis (equal); Investigation (equal); Methodology (equal); Software (supporting); Supervision (supporting); Validation (equal); Visualization (equal); Writing – review & editing (equal). **K. Kurzer-Ogul:** Data curation (equal); Formal analysis (equal); Investigation (equal); Methodology (equal); Software (equal); Validation (equal); Visualization (equal); Writing – review & editing (equal). **S. Pandolfi:** Conceptualization (equal); Formal analysis (equal); Investigation (equal); Methodology (equal); Supervision (supporting); Validation (equal); Writing – review & editing (equal). **D. S. Montgomery:** Conceptualization (equal); Investigation (equal); Methodology (equal); Supervision (equal); Validation (equal); Visualization (equal); Writing – review & editing (equal). **J. Shang:** Conceptualization (equal); Funding acquisition (equal); Investigation (equal); Supervision (equal); Validation (equal); Writing – review & editing (equal). **H. Aluie:** Conceptualization (equal); Funding acquisition (equal); Investigation (equal); Supervision (equal); Validation (equal); Writing – review & editing (equal). **S. Marchesini:** Methodology (equal); Software (equal); Writing – review & editing (equal). **Y. Liu:** Conceptualization (equal); Formal analysis (equal); Investigation (equal); Methodology (equal); Resources (equal); Writing – review & editing (equal). **K. Li:** Conceptualization (equal); Formal analysis (equal); Investigation (equal); Methodology (equal); Resources (equal); Writing – review & editing (equal). **A. Sakdinawat:** Conceptualization (equal); Formal analysis (equal); Methodology (equal); Resources (equal); Writing – review & editing (equal). **E. C. Galtier:** Conceptualization (equal); Data curation (equal); Investigation (equal); Methodology (equal); Resources (equal); Software (equal); Writing – review & editing (equal). **B. Nagler:** Conceptualization (equal); Data curation (equal); Investigation (equal); Methodology (equal); Resources (equal); Software (equal); Writing – review & editing (equal). **H. J. Lee:** Conceptualization (equal); Data curation (equal); Investigation (equal); Methodology (equal); Resources (equal); Software (equal); Writing – review & editing (equal). **E. F. Cunningham:** Conceptualization (equal); Data curation (equal); Investigation (equal); Methodology (equal); Resources (equal); Software (equal); Writing – review & editing (equal). **T. E. Carver:** Resources (equal); Writing – review & editing (equal). **C. A. Bolme:** Conceptualization (equal); Methodology (equal); Resources (equal); Writing – review & editing (equal). **K. J. Ramos:** Conceptualization (equal); Methodology (equal); Resources (equal); Writing – review & editing (equal). **D. Khaghani:** Conceptualization (equal); Data curation (equal); Investigation (equal); Methodology (equal); Resources (equal); Software (equal); Writing – review & editing (equal). **P. M. Kozlowski:** Conceptualization (equal); Formal analysis (equal); Investigation (equal); Methodology (equal); Validation (equal); Writing – review & editing (equal). **A. Gleason:** Conceptualization (lead); Formal analysis (equal); Funding acquisition (lead);

Investigation (equal); Methodology (equal); Project administration (lead); Resources (equal); Supervision (lead); Validation (equal); Writing – review & editing (equal). **R. L. Sandberg:** Conceptualization (equal); Funding acquisition (equal); Investigation (equal); Methodology (equal); Project administration (equal); Resources (equal); Supervision (equal); Writing – original draft (equal); Writing – review & editing (equal).

DATA AVAILABILITY

The data that support the findings of this study are available from the corresponding author upon reasonable request.

APPENDIX A: ADDITIONAL CONSIDERATIONS FOR XPC IMAGE FORMATION

In the following subsections, we discuss the Fresnel equation definitions and how it relates to the Fresnel definition given in the main text, the construction of the transmission function given the x-ray index of refraction, and the propagation kernels and their associated sampling conditions for simulations. These definitions are critical in producing an accurate forward model corresponding to the experiment.

1. Fresnel equation definitions

A key parameter to consider in an XPC imaging setup is the Fresnel number, Fr , given by⁴⁰

$$Fr = \frac{a^2}{z\lambda}, \quad (\text{A1})$$

where a represents the characteristic length scale of the object. This can correspond to the smallest relevant feature (e.g., the size of a single pixel) or the largest (e.g., the size of the illuminated object or field of view).⁴⁰ Here, z is the sample-to-detector distance and λ is the laser wavelength. If one chooses to utilize the smallest relevant feature, the Fresnel number can be written as

$$Fr = \frac{dx^2}{z\lambda}, \quad (\text{A2})$$

where dx is the effective pixel size, z is the sample-to-detector distance, and λ is the central XFEL wavelength. Assuming the paraxial approximation⁵⁰ and Fresnel scaling theorem,⁵¹ one can then arrive at the effective Fresnel number as defined in Eq. (2) in the main text.

2. Transmission function components

For x-rays at a central wavelength λ , the physical properties of an object are encoded in the 3D complex refractive index distribution

$$n(x, y, z) = 1 - \delta(x, y, z) + i\beta(x, y, z), \quad (\text{A3})$$

where i is the imaginary unit and (x, y, z) describes the 3D spatial coordinates. Here, $\delta(x, y, z) \in \mathbb{R}$ is the refractive index decrement, which characterizes the object's phase shifting properties, and $\beta(x, y, z) \in \mathbb{R}$ denotes the absorption, which describes the attenuation of x-rays within the object. In this work, we assume the

projection approximation^{56,84} as outlined by Paganin⁵¹ indicating that we consider only the projection of the refractive indices over the object thickness L in the x-ray beam direction, which we define to be along z . This approximation is valid since $\lambda^2 |\vec{f}|^2 \ll 1$ ($0.000\,011\,356\,8 \ll 1$)⁸⁴ and/or $z_{\text{eff}}/dx_{\text{eff}} \gg N$ ($1\,436\,614 \gg 2560$).⁵⁶ Here, λ is the laser wavelength, f are the spatial frequency coordinates, z_{eff} is the effective propagation distance, N is the number of pixels along the largest dimension, and dx_{eff} is the effective pixel size. With this assumption, we can define the transmission function $T(x, y)$ of our object as

$$T(x, y) = \exp\left(ik \int_0^L n(x, y, z) - 1 dz\right), \quad (\text{A4})$$

where k is the wavenumber, defined as $2\pi/\lambda$. Inserting Eq. (A3) into Eq. (A4), we obtain the following expression:

$$T(x, y) = \exp\left(-ik \int_0^L \delta(x, y, z) - i\beta(x, y, z) dz\right). \quad (\text{A5})$$

To condense this equation, we define equations for $\phi(x, y)$ and $\mu(x, y)$ as

$$\phi(x, y) = -k \int_0^L \delta(x, y, z) dz, \quad (\text{A6})$$

and

$$\mu(x, y) = k \int_0^L \beta(x, y, z) dz, \quad (\text{A7})$$

which are used to construct Eq. (3) in the main text.

3. Propagation kernel for XPC images

The generation of an in-line XPC image is modeled by propagating $\psi_{EW}(x, y)$ in Eq. (4) to the detector and computing the squared modulus of the resulting wavefield. A common way to propagate the object to the detector plane is to consider the convolutional form of the Fresnel diffraction formula written as⁵⁶

$$\psi_{\text{detector}}(x, y) = \psi_{EW}(x, y) \otimes h(x, y), \quad (\text{A8})$$

where $\psi_{\text{detector}}(x, y)$ is the complex electric field in the detector plane. Here, $h(x, y)$ is the Fresnel impulse response (IR) and is defined as⁵⁶

$$h(x, y) = \frac{e^{ikz_{12}}}{i\lambda z_{12}} \exp\left(\frac{ik}{2z_{12}}(x^2 + y^2)\right), \quad (\text{A9})$$

where (x, y) are the transverse 2D spatial coordinates. The validity of using Eq. (A9) depends on the sampling condition $Fr_{\text{eff}} \leq 1/N$, where N is the number of pixels along the largest dimension⁵⁶ and is violated given our experimental parameters and our N value of 2560. Therefore, instead of directly implementing the Fresnel IR as expressed in Eq. (A9), we use the Fresnel transfer function (TF) with the sampling condition given as $Fr_{\text{eff}} \geq 1/N$. This approach ensures accurate sampling and propagation under our experimental conditions. The Fresnel TF is derived by taking the Fourier transform of Eq. (A9), resulting in⁵⁶

$$H(f_x, f_y) = \mathcal{F}[h(x, y)] = e^{ikz_{12}} \exp(-i\pi\lambda z_{12}(f_x^2 + f_y^2)). \quad (\text{A10})$$

Here, (f_x, f_y) is defined as the 2D spatial frequency coordinates corresponding to (x, y) . By using Eq. (2), we can express Eq. (A10) in terms of the effective Fresnel number, obtaining Eq. (5) in the main text.

APPENDIX B: PHASE RETRIEVAL OF A STATIC VOID AND SHOCKED VOID

This section shows the applications of the CTF-fADMM and PGD phase retrieval algorithms applied to the dataset given in the manuscript by Leong *et al.*³⁹ This dataset is different in the sense that the physical parameters of the void are $d_{out} = 40.88\mu\text{m}$ and the shell thickness is $4.16\mu\text{m}$, which corresponds to a smaller but more thick void than what was presented in Sec. IV. Additionally, there was a different XFEL pulse delay time compared to the XPC images shown in the main manuscript, so the shock wave arrived later.

1. Static void

Applied here are the same principles that were used in the main manuscript to generate synthetic images that closely correspond to the experimental parameters and physical void parameters. Similarly, the CTF-fADMM and PGD methods to reconstruct the phase are used (see Figs. 22 and 25). In the static CTF-fADMM reconstruction, the phase range was set between -3 and 3 , with

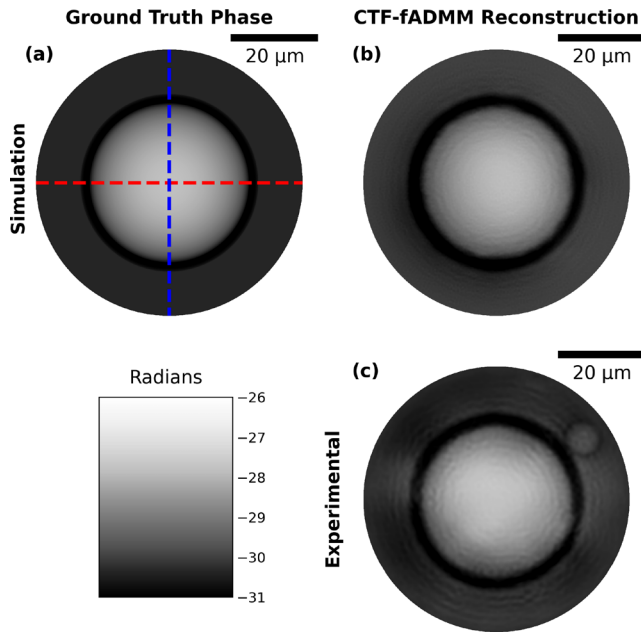


FIG. 22. Comparisons between the 2D ground truth phase and the associated CTF-fADMM reconstructions of the synthetic XPC static image and experimental XPC static image. The blue and red dashed lines correspond to the lineouts in Figs. 23 and 24. (a) Ground truth phase generated using Eq. (12). (b) CTF-fADMM phase reconstruction of the synthetic XPC static image produced as described in Sec. IV. (c) CTF-fADMM phase reconstruction of the experimental XPC static image.

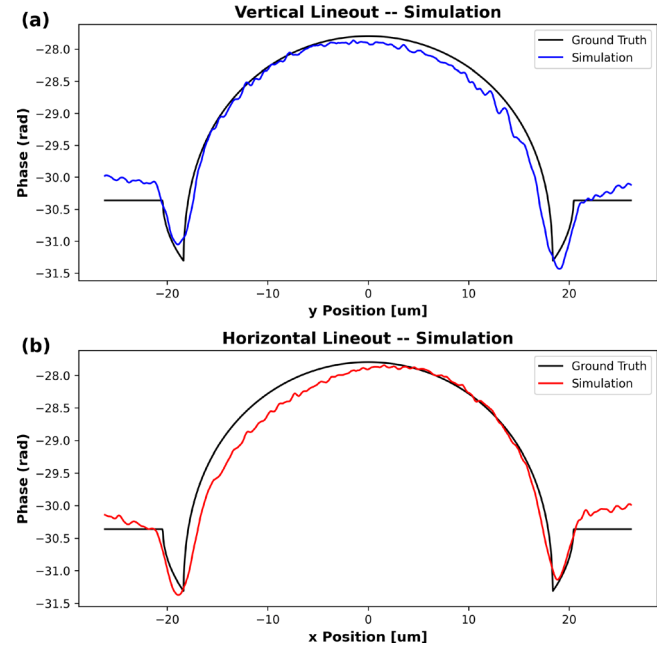


FIG. 23. (a) Vertical (blue) and (b) horizontal (red) lineout comparisons between the simulated static CTF-fADMM phase reconstructions and the ground truth phase (black).

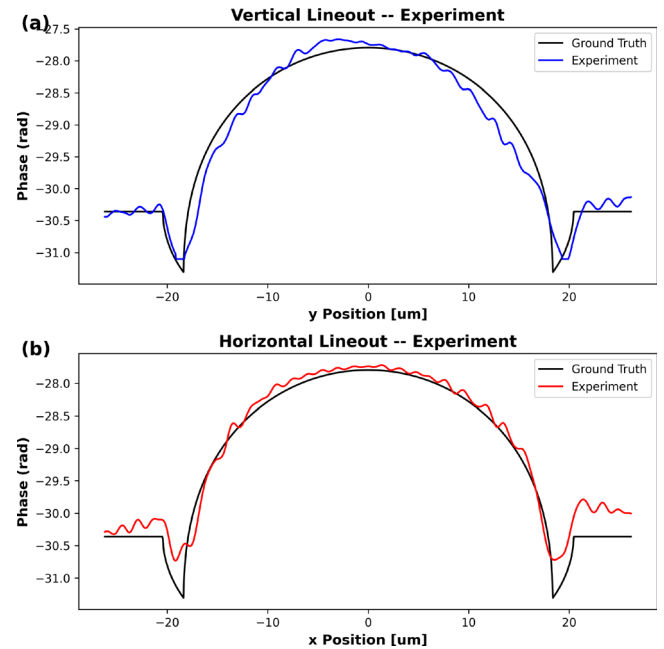


FIG. 24. (a) Vertical and (b) horizontal lineout comparisons between the experimental CTF-fADMM phase reconstructions and the ground truth phase (black).

$\rho = 1 \times 10^{-4}$. For the PGD method, the parameters for the synthetic and experimental static images are listed in Tables III and IV. The phase seed and XPC images were both downsampled by a factor of 4.

TABLE III. Parameters used in the PGD algorithm to reconstruct the synthetic XPC static image. A description of these parameters can be found in the work of Dora *et al.*⁴²

Parameters	Stage 1	Stage 2	Stage 3
Iterations	500	700	5000
Upsampling (S^\dagger)	2	2	1
Nesterov's momentum (γ)	1.0	1.0	1.0
Update rate (η)	1.1	1.1	1.2
L_2 weight (β)	0	0	0
ϕ smoothing (σ_ϕ)	3.0	1.0	2.0
μ smoothing (σ_μ)	0	0	0
Fourier smoothing (σ_{Fourier})	200	200	0

TABLE IV. Parameters used in the PGD algorithm to reconstruct the experimental XPC static image. A description of these parameters can be found in the work of Dora *et al.*⁴²

Parameters	Stage 1	Stage 2	Stage 3
Iterations	500	700	5000
Upsampling (S^\dagger)	2	2	1
Nesterov's momentum (γ)	1.0	1.0	1.0
Update rate (η)	1.1	1.1	1.1
L_2 weight (β)	0	0	0
ϕ smoothing (σ_ϕ)	2.0	2.0	2.0
μ smoothing (σ_μ)	0	0	0
Fourier smoothing (σ_{Fourier})	128	64	0

2. Shocked void

In the dynamic CTF-fADMM reconstructions, the phase range was set between -15 and -75 , with $\rho = 8 \times 10^{-4}$ (see Fig. 28). For the PGD method, the parameters for the synthetic and experimental dynamic images are listed in Tables V and VI (see Fig. 31). The phase seed and XPC images were both downsampled by a factor of 4.

APPENDIX C: CONSTRUCTING THE SYNTHETIC XPC IMAGE ILLUMINATION FUNCTION

Assuming a Gaussian illumination profile, we estimate $\psi_0(x, y)$ by performing a 2D Gaussian fit on all white field images (x-ray beam without the sample, ~ 112 images per dataset) corresponding to the experimentally recorded static and dynamic XPC images. Due to variations in illumination conditions, including amplitude fluctuations and pointing stability between images in these datasets, we construct two distinct illumination functions for $\psi_0(x, y)$: $\psi_{0,s}(x, y)$ for the static XPC images and $\psi_{0,d}(x, y)$ for the dynamic XPC images. The 2D Gaussian fit yields a full width at half maximum (FWHM) of $\sim 89 \mu\text{m}$ in both white-field datasets. Qualitative analysis indicates that the XFEL beam is best represented by a super-Gaussian of order 0.65, exhibiting a more rapid intensity decay outward from the center compared to a conventional Gaussian. Therefore, we used a super-Gaussian using the same

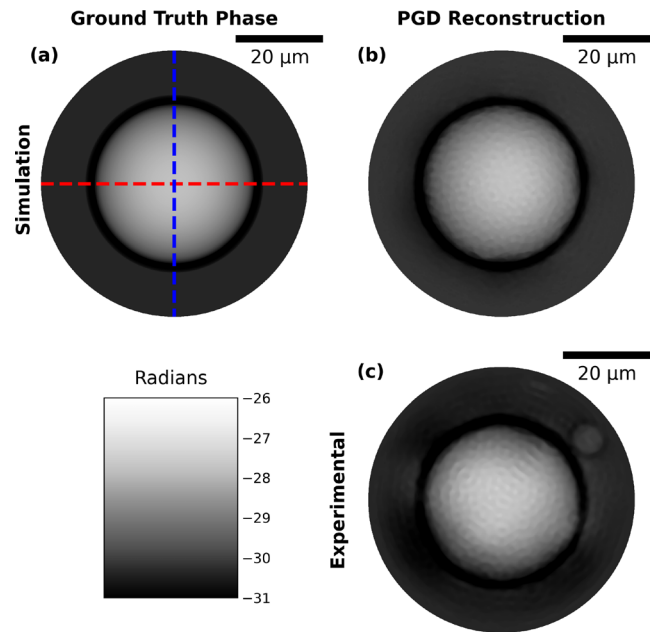


FIG. 25. Comparisons between the 2D ground truth phase and the associated PGD reconstructions of the synthetic XPC static image and experimental XPC static image. The blue and red dashed lines correspond to the lineouts in Figs. 26 and 27. (a) Ground truth phase generated using Eq. (12). (b) PGD phase reconstruction of the synthetic XPC static image using the synthetic CTF-fADMM phase reconstruction as a seed. (c) PGD phase reconstruction of the experimental XPC static image using the experimental CTF-fADMM phase reconstruction as a seed.

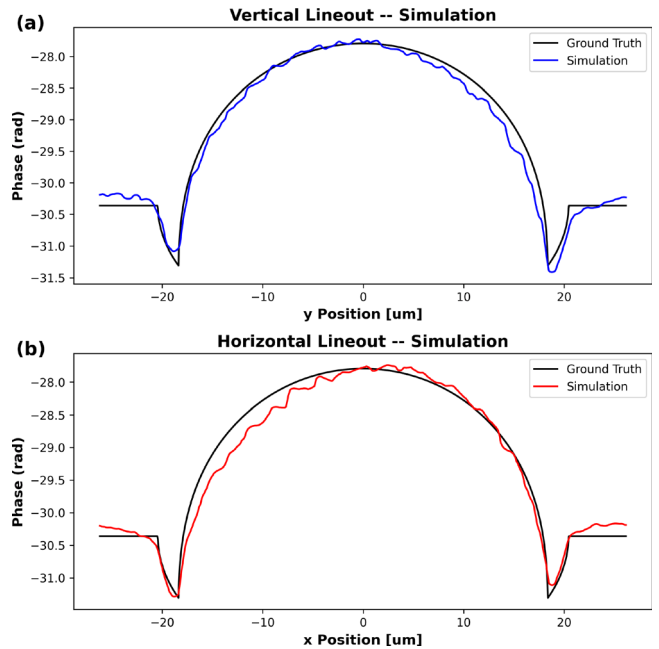


FIG. 26. (a) Vertical (blue) and (b) horizontal (red) lineout comparisons between the simulated static PGD phase reconstructions and the ground truth phase (black).

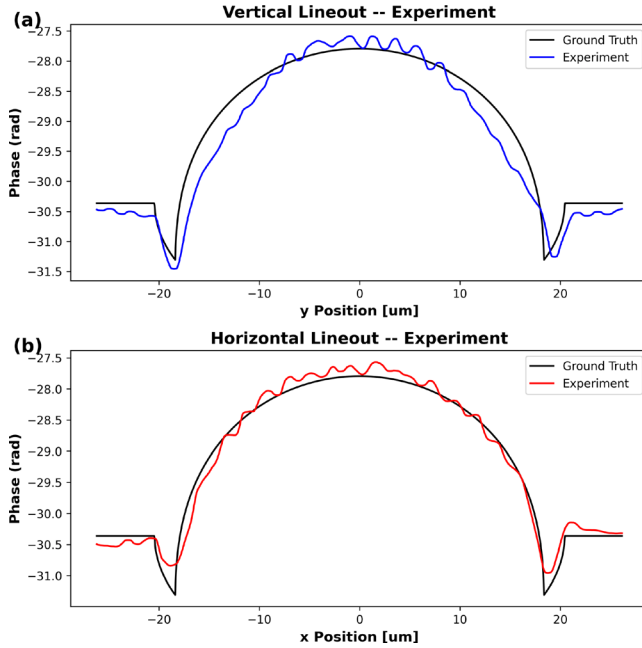


FIG. 27. (a) Vertical (blue) and (b) horizontal (red) lineout comparisons between the experimental static phase reconstructions and the ground truth phase (black).

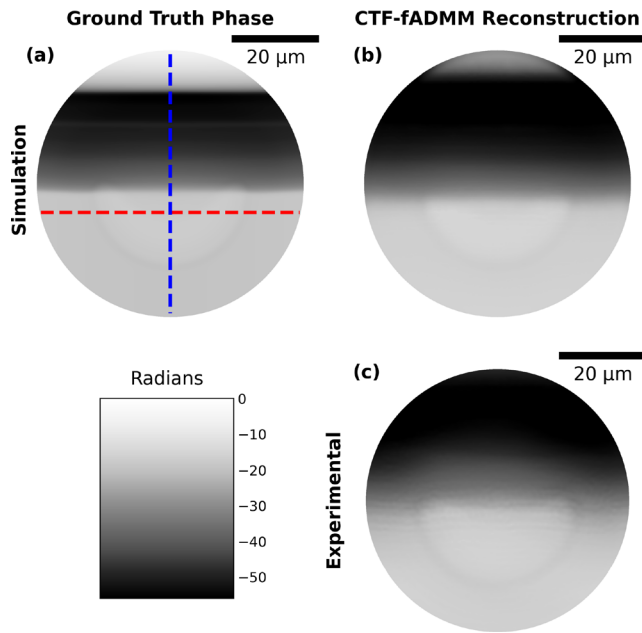


FIG. 28. Comparisons between the 2D ground truth phase and the associated CTF-fADMM reconstructions of the synthetic XPC dynamic image and experimental XPC dynamic image at a later void-collapse stage. The blue and red dashed lines correspond to the lineouts in Figs. 29 and 30. (a) Ground truth phase generated using xRAGE. (b) CTF-fADMM phase reconstruction of the synthetic XPC dynamic image. (c) CTF-fADMM phase reconstruction of the experimental XPC dynamic image.

TABLE V. Parameters used in the PGD algorithm to reconstruct the synthetic XPC dynamic image at a later collapse stage. A description of these parameters can be found in the work of Dora *et al.*⁴²

Parameters	Stage 1	Stage 2	Stage 3	Stage 4
Iterations	1000	500	600	1500
Upsampling (S^\dagger)	2	2	1	1
Nesterov's momentum (γ)	1.0	1.0	1.0	1.0
Update rate (η)	1.1	1.1	1.1	1.1
L_2 weight (β)	0	0	0	0
ϕ smoothing (σ_ϕ)	4.0	2.0	2.0	2.0
μ smoothing (σ_μ)	0	0	0	0
Fourier smoothing (σ_{Fourier})	64	12	12	0

TABLE VI. Parameters used in the PGD algorithm to reconstruct the experimental XPC dynamic image at a later void collapse stage. A description of these parameters can be found in the work of Dora *et al.*⁴²

Parameters	Stage 1	Stage 2	Stage 3	Stage 4
Iterations	700	300	500	2500
Upsampling (S^\dagger)	2	2	1	1
Nesterov's momentum (γ)	1.0	1.0	1.0	1.0
Update rate (η)	1.1	1.1	1.1	1.1
L_2 weight (β)	0	0	0	0
ϕ smoothing (σ_ϕ)	2.5	2.5	2.0	2.0
μ smoothing (σ_μ)	0	0	0	0
Fourier smoothing (σ_{Fourier})	32	32	18	0

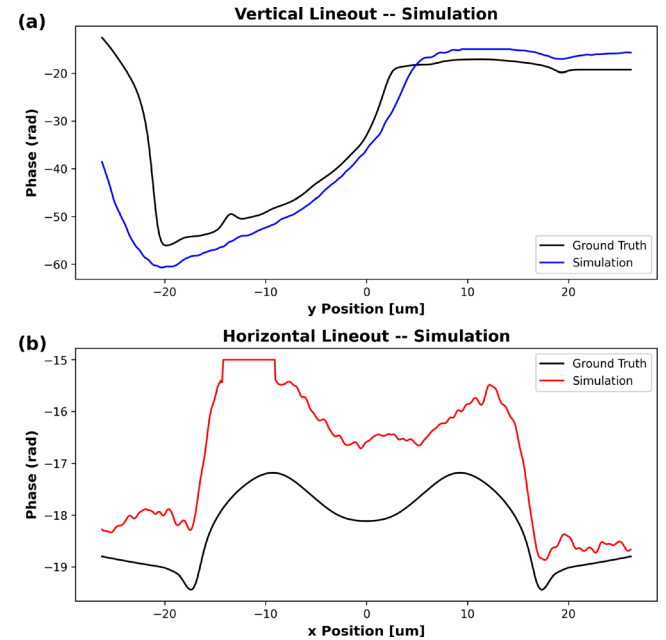


FIG. 29. (a) Vertical (blue) and (b) horizontal (red) lineout comparisons between the simulated dynamic CTF-fADMM phase reconstructions and the ground truth phase (black).

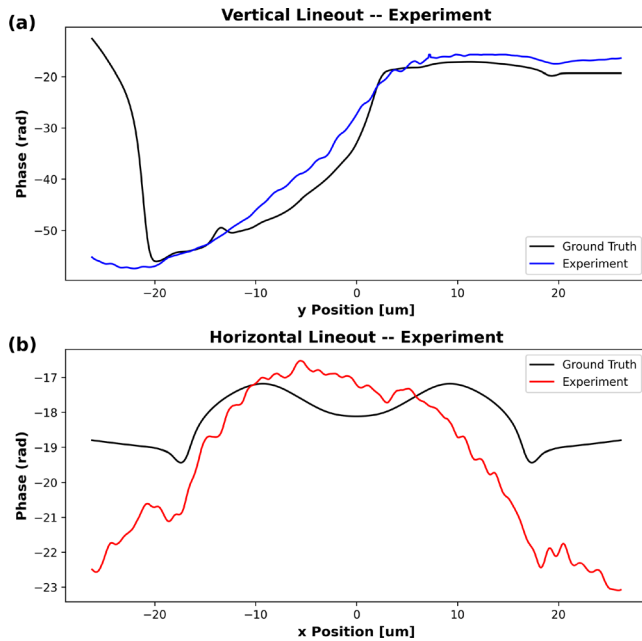


FIG. 30. (a) Vertical (blue) and (b) horizontal (red) lineout comparisons between the experimental CTF-fADMM phase reconstructions and the ground truth phase (black).

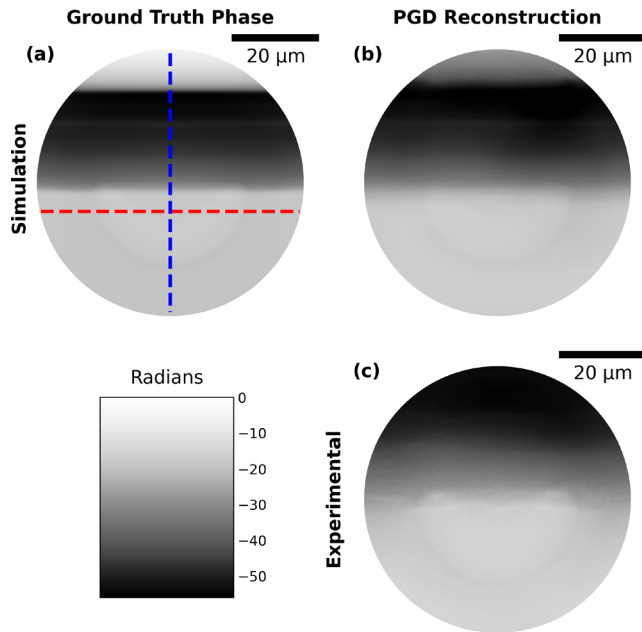


FIG. 31. Comparisons between the 2D ground truth phase and the associated PGD reconstructions of the synthetic XPC dynamic image and experimental XPC dynamic image at a later void-collapse stage. The blue and red dashed lines correspond to the lineouts in Figs. 32 and 33. (a) Ground truth phase generated using xRAGE. (b) PGD phase reconstruction of the synthetic XPC dynamic image using the synthetic CTF-fADMM phase reconstruction as a seed. (c) PGD phase reconstruction of the experimental XPC dynamic image using the experimental CTF-fADMM phase reconstruction as a seed.

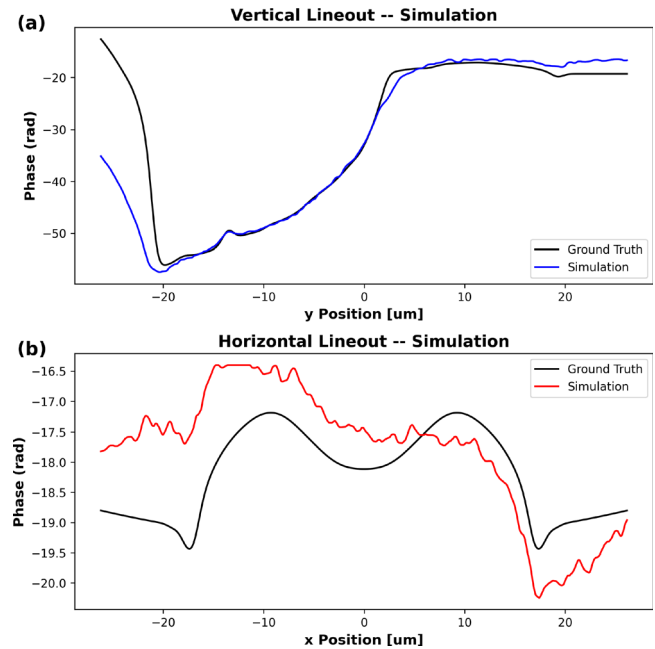


FIG. 32. (a) Vertical (blue) and (b) horizontal (red) lineout comparisons between the simulated dynamic PGD phase reconstructions and the ground truth phase (black).

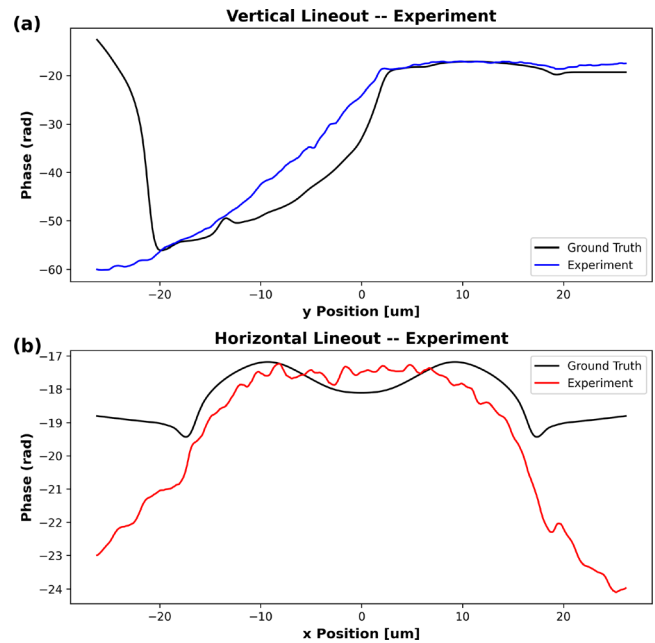


FIG. 33. (a) Vertical (blue) and (b) horizontal (red) lineout comparisons between the experimental dynamic PGD phase reconstructions and the ground truth phase (black).

FWHM from the 2D Gaussian fit. Additionally, the 2D Gaussian fit provides beam amplitudes and shifts in x and y for all white field images. For the static case, peak amplitudes ranged from 16 to 22, whereas for the dynamic case, they ranged from 48 to 62, reflecting

the lower x-ray intensity in the static dataset (10% x-ray transmission) compared to the dynamic dataset (100% x-ray transmission). Beam shifts (pointing stability) ranged from 43.66 nm to a maximum of 3.58 μm , highlighting the extreme variability introduced by the stochastic nature of the XFEL pulses. Finally, to replicate the limited FOV observed in experimental white fields and XPC images, we combine the super-Gaussian illumination function $\psi_{0,\text{superGaussian}}$, which includes the beam shifts, with a top-hat function $\psi_{0,\text{tophat}}$, where edges are smoothed by 20 pixels.

APPENDIX D: PSF AND SAMPLE PARAMETERS

The final forward model considerations are the geometric parameters of the sample and the system's PSF. We model the PSF as a normalized Gaussian

$$G_{\text{PSF}} = \frac{1}{2\pi\sigma^2} \exp\left(-\frac{x^2 + y^2}{2\sigma^2}\right), \quad (\text{D1})$$

where σ is the standard deviation that characterizes the extent of the blurring in the optical system. We adopted this simplified model since we did not perform an experimental measurement of the PSF and it involves only a single parameter to optimize. Although there are more complex PSF models³⁹ that can be employed, we found

that this choice of PSF was sufficient for phase reconstructions presented here.

The physical parameters of the hollow SiO_2 voids were provided by Cospheric LLC, though variations in shell diameter and thickness exist across different samples. To determine the appropriate σ for the PSF and physical parameters for our sample, we employed a least squares minimization scheme

$$\arg \min_{x_c, y_c, d_{\text{out}}, d_{\text{in}}, \sigma} \|I_{\text{experiment}} - I_{\text{simulated}}\|^2. \quad (\text{D2})$$

This method compares a flat-field corrected experimental static image ($I_{\text{experiment}}$) with a synthetic counterpart ($I_{\text{simulated}}$) that is noiseless, unblurred, and free of speckle, following the approach outlined by Leong *et al.*³⁹ In this optimization, the parameters x_c , y_c , d_{out} , and d_{in} were allowed to vary within Eqs. (12) and (13). Their initial values were set to $x_c = 0 \mu\text{m}$, $y_c = 0 \mu\text{m}$, $d_{\text{out}} = 40 \mu\text{m}$, and $d_{\text{in}} = 36.5 \mu\text{m}$. Additionally, within the same minimization scheme, the Gaussian PSF parameter σ from Eq. (D1) was also optimized, initialized at 350 nm based on qualitative agreement with the blur observed in the experimental image. Through this procedure, we refined the void center coordinates to $x_c = 0.8613 \mu\text{m}$ and $y_c = 0.064 \mu\text{m}$, while the outer and inner void diameters were adjusted to $d_{\text{out}} = 42.27 \mu\text{m}$ and $d_{\text{in}} = 40.444 \mu\text{m}$, respectively. The optimized value for the Gaussian PSF σ was determined to be 410.93 nm. These values were used in Eqs. (12), (13), and (D1) when constructing the white field and XPC image forward models. From this minimization procedure, it can be seen that Fig. 34(b) closely corresponds to the blur seen in Fig. 34. The associated lineouts in Figs. 34(c) and 34(d) further support this σ value.

APPENDIX E: DATA PREPROCESSING AND FOV EXTENSIONS

1. PCA vs image registration vs PCA + image registration

Traditional white-field correction (or flat-field correction) methods involve capturing white-fields (flat-fields) before or after sample image acquisition and dividing the sample images by these reference fields. However, due to the stochastic nature of XFEL pulses,^{43,58} this approach is often insufficient, requiring more advanced methods to reduce artifacts in XPC images. One such method involves PCA, which effectively captures XFEL pulse variability and reduces artifacts that are consistent between white fields and sample XPC images. However, in more extreme cases where the presence of a compressive shockwave interacts with a sample, the refraction caused by the shockwave shifts features significantly in the XPC image relative to the white fields. As a result, division of the white fields or generation of a synthetic white field with PCA leads to mismatched features, leaving artifacts in the shocked region. Mismatched features can be seen in Figs. 35(a) and 35(d), where the shocked portion of the sample retained artifacts. However, in the lower unshocked portion, PCA is extremely effective. Therefore, a combination of methods (image registration + PCA) is required for optimal white-field correction and successful phase reconstructions.

One effective solution to mitigate artifacts in the shocked region is to incorporate image registration using the *SimpleITK*

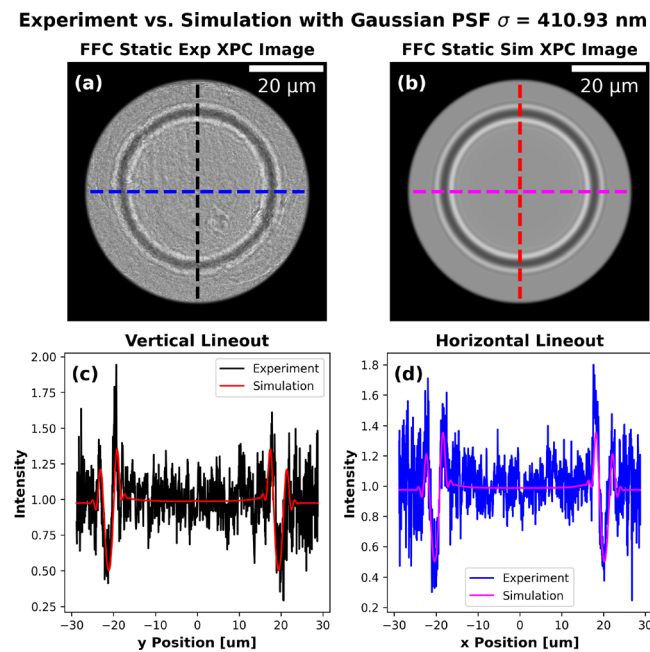


FIG. 34. Comparison between (a) flat-field-corrected (FFC) experimental XPC image and (b) synthetic XPC image after applying Gaussian PSF blur. Lineouts in (c) and (d) demonstrate that a blur kernel with $\sigma = 410.93 \text{ nm}$ applied to the synthetic image closely matches the experimental blur. This value was used in the forward model to generate synthetic datasets. To avoid an inverse crime during deconvolution, σ was re-estimated by reapplying the minimization algorithm to the blurred synthetic image, replicating the experimental scenario in which the PSF is unknown. This independently recovered σ was then used for deconvolution prior to phase retrieval of the synthetic datasets.

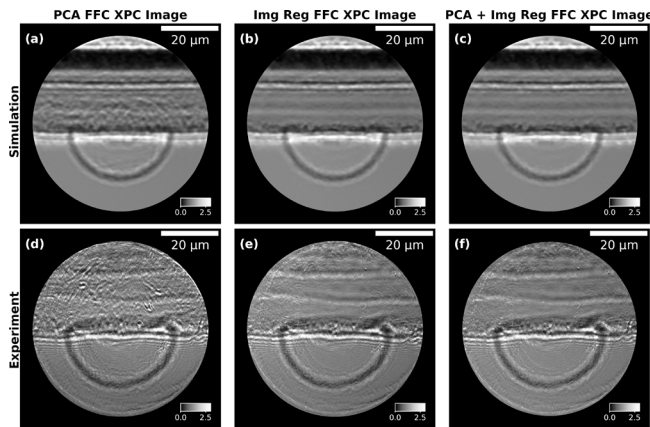


FIG. 35. Flat-field corrected images using PCA only (a, d), image registration only (b, e), and PCA with image registration (c, f). (a) Synthetic FFC XPC image using PCA. The shock region contains artifacts that PCA could not remove because of the large phase gradient caused by the long-pulse laser shockwave. This shifts features significantly in the dynamic XPC image compared to the white fields. (b) Image registration was applied to the simulated dynamic XPC image. Most of the artifacts are mitigated, but the intensity is non-uniform as image registration does not correct for slowly varying fluctuations (e.g., pointing stability and beam shifts). (c) PCA + image registration was applied to the synthetic XPC dynamic image to reduce the artifacts in the shocked region. PCA is used on the image registered white fields to correct for slowly varying fluctuations, which provides a better input into the phase retrieval algorithms. (d)–(f) Same procedure that was used for the synthetic dynamic XPC images was applied to the experimental data. The image in (f) illustrates the effectiveness of combining PCA and image registration instead of using a single method by itself.

python library,^{44,61,62} which aligns white fields to XPC images before being input into PCA for final flat-field correction. Optimal flat-field correction using image registration involves four key stages: selecting a transformation model, a similarity metric, an optimizer, and an interpolator. The transformation model we choose is the “DisplacementFieldTransform.” This enables every pixel in the white fields to be aligned/warped to the best corresponding position in the sample XPC images. We choose the “ANTSNeighborhoodCorrelation” similarity metric due to its robustness against illumination variations. For optimization, we choose the “gradient descent optimizer” due to its balance between registration speed and accuracy. Finally, we employ a “linear interpolator,” as sub-pixel accuracy is essential for image registration. Since transformed coordinates may not align exactly with the original grid, linear interpolation estimates pixel intensities at non-integer positions using a weighted average of neighboring pixels. While higher-order interpolation is possible, it incurs additional computational costs. Linear interpolation strikes a balance between accuracy and efficiency.

Our image registration procedure begins by aligning each white-field image to the first white field, yielding a set of geometrically warped white-field images. These warped white fields are then registered to the corresponding object images (static or dynamic). To correct for illumination amplitude differences between the warped white fields and the object images, we apply a multiplicative intensity normalization during this second registration step. Specifically, we define a mask corresponding to the shared field of

view (FOV) between the white-field and object images, and compute the mean intensity within this region for both images. The white-field image is then scaled by the ratio of these mean values. That is, the mean intensity of the object image divided by that of the white field. This normalization compensates for shot-to-shot fluctuations in illumination and corrects the intensity mismatch between white-field and object images. By rescaling the white-field intensities to match the amplitude scale of the object images, we improve the robustness of the registration algorithm, ensuring more accurate alignment of structural features. This normalization also enables meaningful comparisons between results obtained using image registration alone and those that incorporate both registration and PCA. The resulting intensity-scaled and geometrically warped white-field images are then used as inputs to the PCA algorithm for final flat-field correction.

To further enhance registration accuracy, we implement *SimpleITK*’s multi-resolution scheme, aligning progressively higher-resolution images. Our approach uses downsampling factors of 256, 128, 64, 32, 16, 8, 4, 2, and 1, with corresponding Gaussian smoothing (σ) values of 128, 64, 32, 16, 8, 4, 2, and 1, ensuring smooth transformations at each level. With this method, we achieve significantly improved flat-field correction, producing higher-quality XPC images with fewer artifacts. As shown in Figs. 35(b) and 35(e), image registration results in a flatter, artifact-free image. However, image registration on its own cannot account for the low frequency x-ray beam fluctuations. Therefore, we combine PCA and image registration as seen in Figs. 35(c) and 35(f), which corrects for fast- and slowly varying features. These corrected XPC images serve as the input for phase retrieval algorithms.

REFERENCES

- ¹S. E. H. Murph and M. A. Murph, “Nuclear fusion: The promise of endless energy,” *Phys. Sci. Rev.* **8**, 3095–3118 (2023).
- ²K. Malik, S. C. Capareda, B. R. Kamboj, S. Malik, K. Singh, S. Arya, and D. K. Bishnoi, “Biofuels production: A review on sustainable alternatives to traditional fuels and energy sources,” *Fuels* **5**, 157–175 (2024).
- ³H. Abu-Shawareb, and others (Indirect Drive ICF Collaboration), “Lawson criterion for ignition exceeded in an inertial fusion experiment,” *Phys. Rev. Lett.* **129**, 075001 (2022).
- ⁴H. Abu-Shawareb, and others (Indirect Drive ICF Collaboration), “Achievement of target gain larger than unity in an inertial fusion experiment,” *Phys. Rev. Lett.* **132**, 065102 (2024).
- ⁵A. L. Kritcher, A. B. Zylstra, C. R. Weber, O. A. Hurricane, D. A. Callahan, D. S. Clark, L. Divol, D. E. Hinkel, K. Humbird, O. Jones, J. D. Lindl, S. Maclaren, D. J. Strozzi, C. V. Young, A. Allen, B. Bachmann, K. L. Baker, T. Braun, G. Brunton, D. T. Casey, T. Chapman, C. Choate, E. Dewald, J.-M. G. Di Nicola, M. J. Edwards, S. Haan, T. Fehrenbach, M. Hohenberger, E. Kur, B. Kustowski, C. Kong, O. L. Landen, D. Larson, B. J. MacGowan, M. Marinak, M. Millot, A. Nikroo, R. Nora, A. Pak, P. K. Patel, J. E. Ralph, M. Ratledge, M. S. Rubery, D. J. Schlossberg, S. M. Sepke, M. Stadermann, T. I. Suratwala, R. Tommasini, R. Town, B. Woodworth, B. Van Wenterghem, and C. Wild, “Design of the first fusion experiment to achieve target energy gain $G>1$,” *Phys. Rev. E* **109**, 025204 (2024).
- ⁶O. A. Hurricane, D. A. Callahan, D. T. Casey, A. R. Christopherson, A. L. Kritcher, O. L. Landen, S. A. Maclaren, R. Nora, P. K. Patel, J. Ralph, D. Schlossberg, P. T. Springer, C. V. Young, and A. B. Zylstra, “Energy principles of scientific breakeven in an inertial fusion experiment,” *Phys. Rev. Lett.* **132**, 065103 (2024).
- ⁷M. S. Rubery, M. D. Rosen, N. Aybar, O. L. Landen, L. Divol, C. V. Young, C. Weber, J. Hammer, J. D. Moody, A. S. Moore, A. L. Kritcher, A. B. Zylstra, O. Hurricane, A. E. Pak, S. MacLaren, G. Zimmerman, J. Harte, and T. Woods,

- "Hohlraum reheating from burning NIF implosions," *Phys. Rev. Lett.* **132**, 065104 (2024).
- ⁸S. Fujioka, "Nuclear-fusion reaction beats breakeven," *Physics* **17**, 14 (2024).
- ⁹A. Pak, A. B. Zylstra, K. L. Baker, D. T. Casey, E. Dewald, L. Divol, M. Hohenberger, A. S. Moore, J. E. Ralph, D. J. Schlossberg, R. Tommasini, N. Aybar, B. Bachmann, R. M. Bionta, D. Fittinghoff, M. Gatu Johnson, H. Geppert Kleinrath, V. Geppert Kleinrath, K. D. Hahn, M. S. Rubery, O. L. Landen, J. D. Moody, L. Aghaian, A. Allen, S. H. Baxamusa, S. D. Bhandarkar, J. Biener, N. W. Birge, T. Braun, T. M. Briggs, C. Choate, D. S. Clark, J. W. Crippen, C. Danly, T. Döppner, M. Durocher, M. Erickson, T. Fehrenbach, M. Freeman, M. Havre, S. Hayes, T. Hilsabeck, J. P. Holder, K. D. Humbird, O. A. Hurricane, N. Izumi, S. M. Kerr, S. F. Khan, Y. H. Kim, C. Kong, J. Jeet, B. Kozioziemski, A. L. Kritcher, K. M. Lamb, N. C. Lemos, B. J. MacGowan, A. J. Mackinnon, A. G. MacPhee, E. V. Marley, K. Meaney, M. Millot, J.-M. G. D. Nicola, A. Nikroo, R. Nora, M. Ratledge, J. S. Ross, S. J. Shin, V. A. Smalyuk, M. Stadermann, S. Stoupin, T. Suratwala, C. Troselle, B. Van Wenterghem, C. R. Weber, C. Wild, C. Wilde, P. T. Wooddy, B. N. Woodworth, and C. V. Young, "Observations and properties of the first laboratory fusion experiment to exceed a target gain of unity," *Phys. Rev. E* **109**, 025203 (2024).
- ¹⁰E. R. Sadik-Zada, A. Gatto, and Y. Weißnicht, "Back to the future: Revisiting the perspectives on nuclear fusion and juxtaposition to existing energy sources," *Energy* **290**, 129150 (2024).
- ¹¹S. Meschini, F. Laviano, F. Ledda, D. Pettinari, R. Testoni, D. Torsello, and B. Panella, "Review of commercial nuclear fusion projects," *Front. Energy Res.* **11**, 1157394 (2023).
- ¹²C. Paz-Soldan, E. Belonohy, T. Carter, L. E. Cote, E. Kostadinova, C. Lowe, S. L. Sharma, S. de Clark, J. Deshpande, K. Kelly, V. Kruse, B. Makani, D. A. Schaffner, and K. E. Thome, "Accelerating the fusion workforce," *arXiv:2501.03372* (2025).
- ¹³M. Greenwald, U. Shumlak, and D. T. Anderson, "Preface to special issue: Private fusion research: Opportunities and challenges in plasma science," *Phys. Plasmas* **31**, 090401 (2024).
- ¹⁴T. I. Chapman and N. R. Walkden, "An overview of shared technical challenges for magnetic and inertial fusion power plant development," *Phil. Trans. R. Soc. A* **379**, 20200019 (2021).
- ¹⁵D. S. Clark, A. Allen, S. H. Baxamusa, J. Biener, M. M. Biener, T. Braun, S. Davidovits, L. Divol, W. A. Farmer, T. Fehrenbach, C. Kong, M. Millot, J. Milovich, A. Nikroo, R. C. Nora, A. E. Pak, M. S. Rubery, M. Stadermann, P. Sterne, C. R. Weber, and C. Wild, "Modeling ablator defects as a source of mix in high-performance implosions at the National Ignition Facility," *Phys. Plasmas* **31**, 062706 (2024).
- ¹⁶D. S. Clark, M. M. Marinak, C. R. Weber, D. C. Eder, S. W. Haan, B. A. Hammel, D. E. Hinkel, O. S. Jones, J. L. Milovich, P. K. Patel, H. F. Robey, J. D. Salmonson, S. M. Sepke, and C. A. Thomas, "Radiation hydrodynamics modeling of the highest compression inertial confinement fusion ignition experiment from the National Ignition Campaign," *Phys. Plasmas* **22**, 022703 (2015).
- ¹⁷V. A. Smalyuk, S. V. Weber, D. T. Casey, D. S. Clark, J. E. Field, S. W. Haan, B. A. Hammel, A. V. Hamza, D. E. Hoover, O. L. Landen, A. Nikroo, H. F. Robey, and C. R. Weber, "Hydrodynamic instability growth of three-dimensional, 'native-roughness' modulations in x-ray driven, spherical implosions at the National Ignition Facility," *Phys. Plasmas* **22**, 072704 (2015).
- ¹⁸S. J. Ali, P. M. Celliers, S. W. Haan, T. R. Boehly, N. Whiting, S. H. Baxamusa, H. Reynolds, M. A. Johnson, J. D. Hughes, B. Watson, K. Engelhorn, V. A. Smalyuk, and O. L. Landen, "Hydrodynamic instability seeding by oxygen non-uniformities in glow discharge polymer inertial fusion ablaters," *Phys. Rev. E* **98**, 033204 (2018).
- ¹⁹Y. X. Liu, Z. Chen, L. F. Wang, Z. Y. Li, J. F. Wu, W. H. Ye, and Y. J. Li, "Dynamic of shock-bubble interactions and nonlinear evolution of ablative hydrodynamic instabilities initiated by capsule interior isolated defects," *Phys. Plasmas* **30**, 042302 (2023).
- ²⁰B. M. Haines, J. P. Sauppe, B. J. Albright, W. S. Daughton, S. M. Finnegan, J. L. Kline, and J. M. Smidt, "A mechanism for reduced compression in indirectly driven layered capsule implosions," *Phys. Plasmas* **29**, 042704 (2022).
- ²¹R. Betti and O. A. Hurricane, "Inertial-confinement fusion with lasers," *Nat. Phys.* **12**, 435–448 (2016).
- ²²J. R. Peterson, B. M. Johnson, and S. W. Haan, "Instability growth seeded by DT density perturbations in ICF capsules," *Phys. Plasmas* **25**, 092705 (2018).
- ²³D. Ranjan, J. Oakley, and R. Bonazza, "Shock-bubble interactions," *Annu. Rev. Fluid Mech.* **43**, 117–140 (2011).
- ²⁴M. Armstrong, E. Bukovsky, W. Shaw, L. Lauderbach, R. Austin, P. Grivickas, R. Hodgins, N. Sinclair, J. Klug, T. Willey, J. Zaug, and L. Fried, "Time-resolved x-ray imaging of void collapse in silicone and TNT," Tech. Rep. LLNL-PROC-763328 (Lawrence Livermore National Lab. (LLNL), Livermore, CA, 2018).
- ²⁵C. J. Blum-Sorensen, C. A. Duarte, J. D. Drake, N. E. Kerschen, K. Fezzaa, M. Koslowski, W. W. Chen, and S. F. Son, "Phase contrast x-ray imaging of the collapse of an engineered void in single-crystal HMX," *Propellants. Explos. Pyrotech.* **47**, e202100297 (2022).
- ²⁶E. M. Escauriza, J. P. Duarte, D. J. Chapman, M. E. Rutherford, L. Farbaniec, J. C. Jonsson, L. C. Smith, M. P. Olbinado, J. Skidmore, P. Foster, T. Ringrose, A. Rack, and D. E. Eakins, "Collapse dynamics of spherical cavities in a solid under shock loading," *Sci. Rep.* **10**, 8455 (2020).
- ²⁷N. Haehn, C. Weber, J. Oakley, M. Anderson, D. Ranjan, and R. Bonazza, "Experimental investigation of a twice-shocked spherical gas inhomogeneity with particle image velocimetry," *Shock Waves* **21**, 225–231 (2011).
- ²⁸J.-F. Haas and B. Sturtevant, "Interaction of weak shock waves with cylindrical and spherical gas inhomogeneities," *J. Fluid Mech.* **181**, 41–76 (1987).
- ²⁹M. Vassholz, H. P. Hoeppe, J. Hagemann, J. M. Rosselló, M. Osterhoff, R. Mettin, T. Kurz, A. Schropp, F. Seiboth, C. G. Schroer, M. Scholz, J. Möller, J. Hallmann, U. Boesenberg, C. Kim, A. Zozulya, W. Lu, R. Shayduk, R. Schaffer, A. Madsen, and T. Salditt, "Pump-probe x-ray holographic imaging of laser-induced cavitation bubbles with femtosecond FEL pulses," *Nat. Commun.* **12**, 3468 (2021).
- ³⁰L. Antonelli, F. Barbato, D. Mancelli, J. Trela, G. Zeraoui, G. Boutoux, P. Neumayer, S. Atzeni, A. Schiavi, L. Volpe, V. Bagnoud, C. Brabetz, B. Zielbauer, P. Bradford, N. Woolsey, B. Borm, and D. Batani, "X-ray phase-contrast imaging for laser-induced shock waves," *Europhys. Lett.* **125**, 35002 (2019).
- ³¹L. Antonelli, W. Theobald, F. Barbato, S. Atzeni, D. Batani, R. Betti, V. Bouffettier, A. Casner, L. Ceurvorst, D. Cao, J. J. Ruby, K. Glize, T. Goudal, A. Kar, M. Khan, A. Dearling, M. Koenig, P. M. Nilson, R. H. Scott, O. Turianska, M. Wei, and N. C. Woolsey, "X-ray phase-contrast imaging of strong shocks on OMEGA EP," *Rev. Sci. Instrum.* **95**, 113504 (2024).
- ³²F. Barbato, S. Atzeni, D. Batani, D. Bleiner, G. Boutoux, C. Brabetz, P. Bradford, D. Mancelli, P. Neumayer, A. Schiavi, J. Trela, L. Volpe, G. Zeraoui, N. Woolsey, and L. Antonelli, "Quantitative phase contrast imaging of a shock-wave with a laser-plasma based X-ray source," *Sci. Rep.* **9**, 18805 (2019).
- ³³P. F. Knapp, J. B. Greenly, P. A. Gourdain, C. L. Hoyt, S. A. Pikuz, T. A. Shelkovenko, and D. A. Hammer, "Quasimonochromatic x-ray backlighting on the Cornell Beam Research Accelerator (COBRA) pulsed power generator)," *Rev. Sci. Instrum.* **81**, 10E501 (2010).
- ³⁴J. Workman, J. Cobble, K. Flippo, D. C. Gautier, D. S. Montgomery, and D. T. Offermann, "Phase-contrast imaging using ultrafast x-rays in laser-shocked materials," *Rev. Sci. Instrum.* **81**, 10E520 (2010).
- ³⁵M. P. Valdivia, D. Stutman, C. Stoeckl, C. Mileham, J. Zou, S. Muller, K. Kaiser, C. Sorce, P. A. Keiter, J. R. Fein, M. Trantham, R. P. Drake, and S. P. Regan, "Implementation of a Talbot-Lau x-ray deflectometer diagnostic platform for the OMEGA EP laser," *Rev. Sci. Instrum.* **91**, 023511 (2020).
- ³⁶S. Pandolfi, T. Carver, D. Hodge, A. F. T. Leong, K. Kurzer-Ogul, P. Hart, E. Galtier, D. Khaghani, E. Cunningham, B. Nagler, H. J. Lee, C. Bolme, K. Ramos, K. Li, Y. Liu, A. Sakdinawat, S. Marchesini, P. M. Kozlowski, C. B. Curry, F.-J. Decker, S. Vetter, J. Shang, H. Alilu, M. Dayton, D. S. Montgomery, R. L. Sandberg, and A. E. Gleason, "Novel fabrication tools for dynamic compression targets with engineered voids using photolithography methods," *Rev. Sci. Instrum.* **93**, 103502 (2022).
- ³⁷D. S. Hodge, A. F. T. Leong, S. Pandolfi, K. Kurzer-Ogul, D. S. Montgomery, H. Alilu, C. Bolme, T. Carver, E. Cunningham, C. B. Curry, M. Dayton, F.-J. Decker, E. Galtier, P. Hart, D. Khaghani, H. J. Lee, K. Li, Y. Liu, K. Ramos, J. Shang, S. Vetter, B. Nagler, R. L. Sandberg, and A. E. Gleason, "Multi-frame, ultrafast, x-ray microscope for imaging shockwave dynamics," *Opt. Express* **30**, 38405–38422 (2022).
- ³⁸K. Kurzer-Ogul, B. M. Haines, D. S. Montgomery, S. Pandolfi, J. P. Sauppe, A. F. T. Leong, D. Hodge, P. M. Kozlowski, S. Marchesini, E. Cunningham, E. Galtier, D. Khaghani, H. J. Lee, B. Nagler, R. L. Sandberg, A. E. Gleason,

- H. Aluie, and J. K. Shang, "Radiation and heat transport in divergent shock-bubble interactions," *Phys. Plasmas* **31**, 032304 (2024).
- ⁵⁹A. F. T. Leong, D. S. Hodge, K. Kurzer-Ogul, S. Marchesini, S. Pandolfi, Y. Liu, J. L. Barber, K. Li, A. Sakdinawat, E. C. Galtier, B. Nagler, H. J. Lee, E. F. Cunningham, T. E. Carver, H. Aluie, J. K. Shang, C. A. Bolme, K. J. Ramos, D. Khaghani, R. L. Sandberg, D. S. Montgomery, P. M. Kozlowski, and A. E. Gleason, "Combined speckle- and propagation-based single shot two-dimensional phase retrieval method," *Opt. Express* **32**, 46939–46957 (2024).
- ⁴⁰L. M. Lohse, A.-L. Robisch, M. Töpperwien, S. Maretzke, M. Krenkel, J. Hagemann, and T. Salditt, "A phase-retrieval toolbox for X-ray holography and tomography," *J. Synchrotron Rad.* **27**, 852–859 (2020).
- ⁴¹P. Villanueva-Perez, F. Arcadu, P. Cloetens, and M. Stampanoni, "Contrast-transfer-function phase retrieval based on compressed sensing," *Opt. Lett.* **42**, 1133–1136 (2017).
- ⁴²J. Dora, M. Möddel, S. Flenner, C. G. Schroer, T. Knopp, and J. Hagemann, "Artifact-suppressing reconstruction of strongly interacting objects in X-ray near-field holography without a spatial support constraint," *Opt. Express* **32**, 10801–10828 (2024).
- ⁴³J. Hagemann, M. Vassholz, H. Hoeppe, M. Osterhoff, J. M. Rosselló, R. Mettin, F. Seiboth, A. Schropp, J. Möller, J. Hallmann, C. Kim, M. Scholz, U. Boesenberg, R. Schaffer, A. Zozulya, W. Lu, R. Shayduk, A. Madsen, C. G. Schroer, and T. Salditt, "Single-pulse phase-contrast imaging at free-electron lasers in the hard X-ray regime," *J. Synchrotron Rad.* **28**, 52–63 (2021).
- ⁴⁴B. C. Lowekamp, D. T. Chen, L. Ibanez, and D. Blezek, "The design of SimpleITK," *Front. Neuroinf.* **7**, 45 (2013).
- ⁴⁵A. L. Kritcher, D. Clark, S. Haan, S. A. Yi, A. B. Zylstra, D. A. Callahan, D. E. Hinkel, L. F. Berzak Hopkins, O. A. Hurricane, O. L. Landen, S. A. MacLaren, N. B. Meezan, P. K. Patel, J. Ralph, C. A. Thomas, R. Town, and M. J. Edwards, "Comparison of plastic, high density carbon, and beryllium as indirect drive NIF ablaters," *Phys. Plasmas* **25**, 056309 (2018).
- ⁴⁶S. W. Haan, H. Huang, M. A. Johnson, M. Stadermann, S. Baxamusa, S. Bhandarkar, A. S. Clark, V. Smalyuk, and H. F. Robey, "Instability growth seeded by oxygen in CH shells on the National Ignition Facility," *Phys. Plasmas* **22**, 032708 (2015).
- ⁴⁷R. Betti and J. Sanz, "Bubble acceleration in the ablative Rayleigh-Taylor instability," *Phys. Rev. Lett.* **97**, 205002 (2006).
- ⁴⁸Y. Gao and L. Cao, "Generalized optimization framework for pixel super-resolution imaging in digital holography," *Opt. Express* **29**, 28805–28823 (2021).
- ⁴⁹B. Nagler, A. Schropp, E. C. Galtier, B. Arnold, S. B. Brown, A. Fry, A. Gleason, E. Granados, A. Hashim, J. B. Hastings, D. Samberg, F. Seiboth, F. Tavella, Z. Xing, H. J. Lee, and C. G. Schroer, "The phase-contrast imaging instrument at the matter in extreme conditions endstation at LCLS," *Rev. Sci. Instrum.* **87**, 103701 (2016).
- ⁵⁰A. Pogany, D. Gao, and S. W. Wilkins, "Contrast and resolution in imaging with a microfocus x-ray source," *Rev. Sci. Instrum.* **68**, 2774–2782 (1997).
- ⁵¹D. Paganin, *Coherent X-Ray Optics* (Oxford University Press, 2006).
- ⁵²R. Heintzmann, L. Loetgering, and F. Wechsler, "Scalable angular spectrum propagation," *Optica* **10**, 1407–1416 (2023).
- ⁵³M. A. Barrios, D. G. Hicks, T. R. Boehly, D. E. Fratanduono, J. H. Eggert, P. M. Celliers, G. W. Collins, and D. D. Meyerhofer, "High-precision measurements of the equation of state of hydrocarbons at 1–10 Mbar using laser-driven shock waves," *Phys. Plasmas* **17**, 056307 (2010).
- ⁵⁴H. Zhang, R. Betti, V. Gopalaswamy, R. Yan, and H. Aluie, "Nonlinear excitation of the ablative Rayleigh-Taylor instability for all wave numbers," *Phys. Rev. E* **97**, 011203 (2018).
- ⁵⁵H. Zhang, R. Betti, R. Yan, and H. Aluie, "Nonlinear bubble competition of the multimode ablative Rayleigh-Taylor instability and applications to inertial confinement fusion," *Phys. Plasmas* **27**, 122701 (2020).
- ⁵⁶D. G. Voelz and M. C. Roggemann, "Digital simulation of scalar optical diffraction: Revisiting chirp function sampling criteria and consequences," *Appl. Opt.* **48**, 6132–6142 (2009).
- ⁵⁷J. Kim, J. G. Kim, H. Ki, C. W. Ahn, and H. Ihee, "Estimating signal and noise of time-resolved X-ray solution scattering data at synchrotrons and XFELs," *J. Synchrotron Rad.* **27**, 633–645 (2020).
- ⁵⁸V. V. Nieuwenhove, J. D. Beenhouwer, F. D. Carlo, L. Mancini, F. Marone, and J. Sijbers, "Dynamic intensity normalization using eigen flat fields in X-ray imaging," *Opt. Express* **23**, 27975–27989 (2015).
- ⁵⁹D. Hodge, S. Pandolfi, Y. Liu, K. Li, A. Sakdinawat, M. Seaberg, P. Hart, E. Galtier, D. Khaghani, S. Vetter, F.-J. Decker, B. Nagler, H. J. Lee, C. Bolme, K. Ramos, P. M. Kozlowski, D. S. Montgomery, T. Carver, M. Dayton, L. Dresselhaus-Marais, S. Ali, R. L. Sandberg, and A. Gleason, "Four-frame ultrafast radiography of a shocked sample at an x-ray free electron laser," in *Proceedings of the OSA Imaging and Applied Optics Congress 2021 (3D, COSI, DH, ISA, pcAOP)* (Optica Publishing Group, 2021), p. DTh7F.2.
- ⁶⁰B. H. Avants, N. J. Tustison, G. Song, P. A. Cook, A. Klein, and J. C. Gee, "A reproducible evaluation of ANTs similarity metric performance in brain image registration," *Neuroimage* **54**, 2033–2044 (2011).
- ⁶¹R. Beare, B. Lowekamp, and Z. Yaniv, "Image segmentation, registration and characterization in R with SimpleITK," *J. Stat. Soft.* **86**, 1–35 (2018).
- ⁶²Z. Yaniv, B. C. Lowekamp, H. J. Johnson, and R. Beare, "SimpleITK image-analysis notebooks: A collaborative environment for education and reproducible research," *J. Digit. Imag.* **31**, 290–303 (2018).
- ⁶³S. H. Chan, R. Khoshabeh, K. B. Gibson, P. E. Gill, and T. Q. Nguyen, "An augmented Lagrangian method for total variation video restoration," *IEEE Trans. Image Process.* **20**, 3097–3111 (2011).
- ⁶⁴F. Wittwer, J. Hagemann, D. Brückner, S. Flenner, and C. G. Schroer, "A phase retrieval framework to directly reconstruct the projected refractive index," *Optica* **9**, 295–302 (2022).
- ⁶⁵A. Burvall, U. Lundström, P. A. C. Takman, D. H. Larsson, and H. M. Hertz, "Phase retrieval in X-ray phase-contrast imaging suitable for tomography," *Opt. Express* **19**, 10359–10376 (2011).
- ⁶⁶G. Pedrini, W. Osten, and Y. Zhang, "Wave-front reconstruction from a sequence of interferograms recorded at different planes," *Opt. Lett.* **30**, 833–835 (2005).
- ⁶⁷P. Bao, F. Zhang, G. Pedrini, and W. Osten, "Phase retrieval using multiple illumination wavelengths," *Opt. Lett.* **33**, 309–311 (2008).
- ⁶⁸M. Sanz, J. A. Picazo-Bueno, J. García, and V. Micó, "Improved quantitative phase imaging in lensless microscopy by single-shot multi-wavelength illumination using a fast convergence algorithm," *Opt. Express* **23**, 21352–21365 (2015).
- ⁶⁹Y. Zhou, J. Wu, J. Suo, X. Han, G. Zheng, and Q. Dai, "Single-shot lensless imaging via simultaneous multi-angle LED illumination," *Opt. Express* **26**, 21418–21432 (2018).
- ⁷⁰F. Wittwer, J. Hagemann, D. Brückner, S. Flenner, and C. G. Schroer, "Phase retrieval framework for direct reconstruction of the projected refractive index applied to ptychography and holography," *Optica* **9**, 295–302 (2022).
- ⁷¹H. M. L. Faulkner and J. M. Rodenburg, "Movable aperture lensless transmission microscopy: A novel phase retrieval algorithm," *Phys. Rev. Lett.* **93**, 023903 (2004).
- ⁷²J. R. Fienup, "Reconstruction of a complex-valued object from the modulus of its Fourier transform using a support constraint," *J. Opt. Soc. Am. A* **4**, 118–123 (1987).
- ⁷³T. Latychevskaia and H.-W. Fink, "Reconstruction of purely absorbing, absorbing and phase-shifting, and strong phase-shifting objects from their single-shot in-line holograms," *Appl. Opt.* **54**, 3925–3932 (2015).
- ⁷⁴J. Miao, D. Sayre, and H. N. Chapman, "Phase retrieval from the magnitude of the Fourier transforms of nonperiodic objects," *J. Opt. Soc. Am. A* **15**, 1662–1669 (1998).
- ⁷⁵T. Latychevskaia and H.-W. Fink, "Solution to the twin image problem in holography," *Phys. Rev. Lett.* **98**, 233901 (2007).
- ⁷⁶T. E. Gureyev, A. Pogany, D. M. Paganin, and S. W. Wilkins, "Linear algorithms for phase retrieval in the Fresnel region," *Opt. Commun.* **231**, 53–70 (2004).
- ⁷⁷M. A. Beltran, D. M. Paganin, K. Uesugi, and M. J. Kitchen, "2D and 3D X-ray phase retrieval of multi-material objects using a single defocus distance," *Opt. Express* **18**, 6423–6436 (2010).
- ⁷⁸J.-P. Guigay, "Fourier transform analysis of Fresnel diffraction patterns and in-line holograms," *Optik (Jena)* **49**, 121–125 (1977).
- ⁷⁹L. D. Turner, B. B. Dhal, J. P. Hayes, A. P. Mancuso, K. A. Nugent, D. Paterson, R. E. Scholten, C. Q. Tran, and A. G. Peele, "X-ray phase imaging: Demonstration of extended conditions with homogeneous objects," *Opt. Express* **12**, 2960–2965 (2004).
- ⁸⁰S. Zabler, P. Cloetens, J.-P. Guigay, J. Baruchel, and M. Schlenker, "Optimization of phase contrast imaging using hard x rays," *Rev. Sci. Instrum.* **76**, 073705 (2005).
- ⁸¹P. Cloetens, W. Ludwig, J. Baruchel, J.-P. Guigay, P. Pernot-Rejmánková, M. Salomé-Pateyron, M. Schlenker, J.-Y. Buffière, E. Maire, and G. Peix, "Hard

- x-ray phase imaging using simple propagation of a coherent synchrotron radiation beam," *J. Phys. D: Appl. Phys.* **32**, A145 (1999).
- ⁸²M. Langer, P. Cloetens, J. Guigay, S. Valton, and F. Peyrin, "Quantitative evaluation of phase retrieval algorithms in propagation based phase tomography," in *Proceedings of the 2007 4th IEEE International Symposium on Biomedical Imaging: From Nano to Macro* (IEEE, 2007), pp. 552–555.
- ⁸³J. Hagemann, M. Töpperwien, and T. Salditt, "Phase retrieval for near-field X-ray imaging beyond linearisation or compact support," *Appl. Phys. Lett.* **113**, 041109 (2018).
- ⁸⁴C. Zuo, J. Li, J. Sun, Y. Fan, J. Zhang, L. Lu, R. Zhang, B. Wang, L. Huang, and Q. Chen, "Transport of intensity equation: A tutorial," *Opt. Lasers Eng.* **135**, 106187 (2020).
- ⁸⁵B. Yu, L. Weber, A. Pacureanu, M. Langer, C. Olivier, P. Cloetens, and F. Peyrin, "Evaluation of phase retrieval approaches in magnified X-ray phase nano computerized tomography applied to bone tissue," *Opt. Express* **26**, 11110–11124 (2018).
- ⁸⁶S. Huhn, L. M. Lohse, J. Lucht, and T. Salditt, "Fast algorithms for nonlinear and constrained phase retrieval in near-field X-ray holography based on Tikhonov regularization," *Opt. Express* **30**, 32871–32886 (2022).
- ⁸⁷T. Goldstein, B. O'Donoghue, S. Setzer, and R. Baraniuk, "Fast alternating direction optimization methods," *SIAM J. Imag. Sci.* **7**, 1588–1623 (2014).
- ⁸⁸D. M. Paganin, V. Favre-Nicolin, A. Mirone, A. Rack, J. Villanova, M. P. Olbinado, V. Fernandez, J. C. da Silva, and D. Pelliccia, "Boosting spatial resolution by incorporating periodic boundary conditions into single-distance hard-x-ray phase retrieval," *J. Opt.* **22**, 115607 (2020).
- ⁸⁹D. Paganin, S. C. Mayo, T. E. Gureyev, P. R. Miller, and S. W. Wilkins, "Simultaneous phase and amplitude extraction from a single defocused image of a homogeneous object," *J. Microsc.* **206**, 33–40 (2002).
- ⁹⁰T. Faragó, R. Spiecker, M. Hurst, M. Zuber, A. Cecilia, and T. Baumbach, "Phase retrieval in propagation-based X-ray imaging beyond the limits of transport of intensity and contrast transfer function approaches," *Opt. Lett.* **49**, 5159–5162 (2024).